E 9863-2
7/31/98

NASA/TM—1998-107249/CH2

Solid Lubrication Fundamentals and Applications

Characterization of Solid Surfaces

Kazuhisa Miyoshi
Lewis Research Center, Cleveland, Ohio

July 1998

The NASA STI Program Office . . . in Profile

Since its founding, NASA has been dedicated to the advancement of aeronautics and space science. The NASA Scientific and Technical Information (STI) Program Office plays a key part in helping NASA maintain this important role.

The NASA STI Program Office is operated by Langley Research Center, the Lead Center for NASA's scientific and technical information. The NASA STI Program Office provides access to the NASA STI Database, the largest collection of aeronautical and space science STI in the world. The Program Office is also NASA's institutional mechanism for disseminating the results of its research and development activities. These results are published by NASA in the NASA STI Report Series, which includes the following report types:

- TECHNICAL PUBLICATION. Reports of completed research or a major significant phase of research that present the results of NASA programs and include extensive data or theoretical analysis. Includes compilations of significant scientific and technical data and information deemed to be of continuing reference value. NASA's counterpart of peer-reviewed formal professional papers but has less stringent limitations on manuscript length and extent of graphic presentations.

- TECHNICAL MEMORANDUM. Scientific and technical findings that are preliminary or of specialized interest, e.g., quick release reports, working papers, and bibliographies that contain minimal annotation. Does not contain extensive analysis.

- CONTRACTOR REPORT. Scientific and technical findings by NASA-sponsored contractors and grantees.

- CONFERENCE PUBLICATION. Collected papers from scientific and technical conferences, symposia, seminars, or other meetings sponsored or cosponsored by NASA.

- SPECIAL PUBLICATION. Scientific, technical, or historical information from NASA programs, projects, and missions, often concerned with subjects having substantial public interest.

- TECHNICAL TRANSLATION. English-language translations of foreign scientific and technical material pertinent to NASA's mission.

Specialized services that complement the STI Program Office's diverse offerings include creating custom thesauri, building customized data bases, organizing and publishing research results . . . even providing videos.

For more information about the NASA STI Program Office, see the following:

- Access the NASA STI Program Home Page at ***http://www.sti.nasa.gov***

- E-mail your question via the Internet to help@sti.nasa.gov

- Fax your question to the NASA Access Help Desk at (301) 621-0134

- Telephone the NASA Access Help Desk at (301) 621-0390

- Write to:
  NASA Access Help Desk
  NASA Center for AeroSpace Information
  800 Elkridge Landing Road
  Linthicum Heights, MD 21090-2934

NASA/TM—1998-107249/CH2

Solid Lubrication Fundamentals and Applications

Characterization of Solid Surfaces

Kazuhisa Miyoshi
Lewis Research Center, Cleveland, Ohio

National Aeronautics and
Space Administration

Lewis Research Center

July 1998

Available from

NASA Center for Aerospace Information
800 Elkridge Landing Road
Linthicum Heights, MD 21090-2934
Price Code: A05

National Technical Information Service
5287 Port Royal Road
Springfield, VA 22100
Price Code: A05

Chapter 2
Characterization of Solid Surfaces

2.1 Introduction

Materials and surface analysis has been practised for a relatively long time and has been a fixture of the field of tribology from the beginning [2.1–2.11]. Fifty or so material and surface analysis techniques exist, yet analysis equipment and techniques are undergoing rapid and constant development in response to user needs. Each technique provides specific measurement results in its own unique way. Interpreting those results to extract information that can help tribologists and lubrication engineers solve technical problems takes years of training. Reaching the level of senior analyst usually takes three to five years.

Materials and surface analysis has made considerable contributions, ranging from fundamental tribology to the design, development, evaluation, and quality control of materials and solid-film lubricants. The principal desiderata of a solid-film lubricant for technical applications, especially aerospace, automotive, and other demanding applications, are low shear strength yet high cohesion and adhesion to the substrate, long-term stability under given operating environmental conditions, and long-term compatibility with the substrate. To understand the benefits provided by solid lubricants, and ultimately to provide better solid lubrication, it is necessary to characterize the physical, chemical, topographical, mechanical, and tribological properties of solid lubricants and substrates. These properties must not be seriously affected by environmental conditions, in particular elevated temperatures, vacuum, ions, radiation, gases, particulates, and water.

Although it is now not always the case, characterization problems must be approached from the end of the tribologists, materials users, and lubrication engineers rather than from that of an analytical technique expert. Currently, materials and surface analytical techniques are used mostly either in quality assurance and control of parts and components used in tribology or in investigation of the mechanisms of friction, lubrication, wear, and tribological failures.

This chapter describes powerful analytical techniques capable of sampling tribological surfaces and solid-film lubricants. Some of these techniques may also be used to determine the locus of failure in a bonded structure or coated substrate; such information is important when seeking improved adhesion between a

solid-film lubricant and a substrate and when seeking improved performance and long life expectancy of solid lubricants. Many examples are given here and throughout the book on the nature and character of solid surfaces and their significance in lubrication, friction, and wear. The analytical techniques used include the latest spectroscopic methods.

2.2 Nature and Structure of Real Surfaces

A surface, by definition, is an interface, a marked discontinuity from one material to another. Because no change in nature is ever instantaneous, any real surface has a finite depth, and in characterizing a surface one must at some point consider just what this depth is.

Almost every industrial process involves—even depends on—the behavior of a surface. The surface region, which affects a broad spectrum of properties such as surface energy and tension, adhesion, bonding, friction, lubrication, wear, contamination, oxidation, corrosion, chemical activity, deformation, and fracture, encompasses the first few hundred atomic layers. All surfaces obey the laws of physics and chemistry in their formation, reactions, and combinations. Because any major discontinuity in the solid affects the electronic energy states, effects also arise from surface energy and tension.

Figure 2.1 depicts the surface structure and chemistry of a solid-film lubricant exposed to a surrounding environment and to a bulk substrate material. The solid-film-lubricated surface region includes (1) the single-crystal bulk substrate with defects or the polycrystalline bulk substrate with grain boundaries, (2) a worked layer and an oxide layer, (3) the solid-film lubricant, (4) another oxide layer covered by adsorbed contaminants, and (5) the surrounding environmental species. To understand this surface region, it is first necessary to know how the individual parts (1) to (4) perform in the tribological process. Thus, the nature and properties of parts (1), (2), and (4) are discussed, using examples, in this section.

2.2.1 Bulk Materials

Almost all surfaces of bulk substrate materials that are prepared by mechanical preparation techniques contain defects resulting from plastic deformation, fracture, heating, and contamination. Even cleavage faces are rarely defect free.

Metals and polymers readily deform plastically. Ceramics, while having high strength and high elastic modulus, are normally brittle and fracture with little or no evidence of plastic flow. However, plastic flow has been observed in the surface layers of several ceramics in solid-state contact under load and relative motion. These include magnesium oxide [2.12], aluminum oxide [2.13], manganese-zinc ferrites [2.14], and silicon carbide [2.15] under relatively modest conditions of rubbing contact.

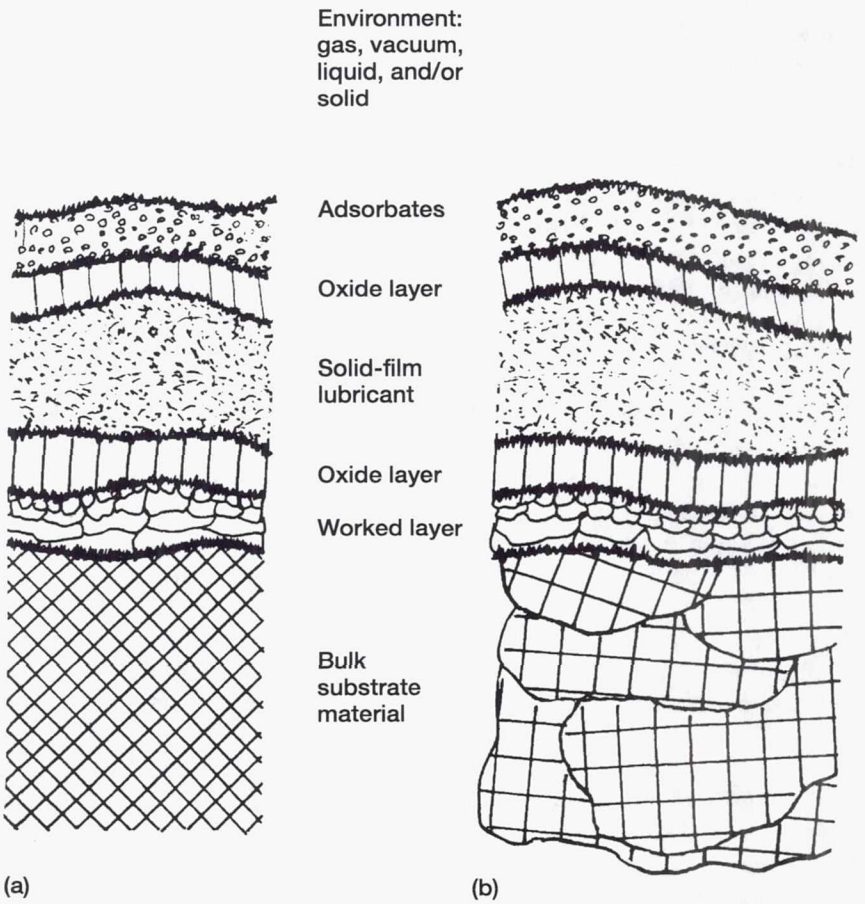

Figure 2.1.—Schematic diagram representing solid-film-lubricated surface region. (a) Single-crystal substrate. (b) Polycrystalline substrate.

Single-Crystal Materials

Properties of a single crystal, such as atomic density, spacing of atomic planes, surface energy, modulus of elasticity, slip systems, influence of imperfections, deformation, fracture, hardness, coefficient of friction, and wear rate, have all been related to crystal orientation. Some examples of the tribological behavior and properties of single crystals are discussed here.

The simplest type of solid surface is a cleavage face of a single crystal. This surface, a regular array of atoms, is flat and smooth. As an example, Fig. 2.2 presents the bulk microstructure and crystallinity of cleaved single-crystal molybdenite. The transmission electron micrograph and transmission electron diffraction pattern reveal homogeneous crystalline and regularly arrayed diffraction spots, indicating a single-crystal structure.

Indentation deformation.—Figure 2.3 shows the distribution of dislocation etch pits on a well-defined single-crystal magnesium oxide (MgO) surface [2.16–2.18]. The MgO bulk crystals were first cleaved along the {001} surface in air and then subjected to hardness indentation or cavitation erosion, which introduced a certain amount of plastic deformation into the {001} surface. Next, the MgO surfaces were chemically etched in a solution of five parts saturated ammonium chloride, one part sulfuric acid, and one part distilled water at room temperature. Then scanning electron micrographs were taken of the etched surfaces. The dislocation-etch-pit pattern on the surface exposed to cavitation (Fig. 2.3(b)) is definitely different from that on the indented surface (Fig. 2.3(a)).

In Fig. 2.3(a) the dislocation-etch-pit pattern around the hardness indentation on the {001} surface contains screw dislocations in the ⟨001⟩ directions ([100] and [010]) and edge dislocations in the ⟨011⟩ directions ([110] and [1$\bar{1}$0]). The screw and edge dislocation arrays are 4.9 and 7.7 times wider, respectively, than the average length of the two diagonals of hardness indentation. On the other hand, a cross-shaped deformation, which contains no edge dislocations, can be seen in Fig. 2.3(b). Similar observations were reported by J. Narayan [2.19, 2.20], who used optical and transmission electron microscopy to investigate the plastic damage introduced into MgO single crystals by bombardment with aluminum oxide (Al_2O_3) particles. He indicated that most of the damage was dislocation dipoles and that, because the resolved stress on $\{110\}_{90°}$ was small, the dislocation-etch-pit pattern was elongated along the ⟨110⟩ directions. His results are consistent with the results presented in Fig. 2.3(b).

After an MgO {001} surface was exposed to cavitation erosion, the MgO bulk crystal was cleaved along a {001} surface perpendicular to the {001} surface exposed to cavitation. And finally all surfaces of the MgO crystal were chemically etched. In Fig. 2.4, which shows a cross section of the cavitation-damaged area, the dislocation rows intersect the specimen surface at 45° and cross the dislocation rows of the other set of $\{110\}_{45°}$ planes.

Explanations for the slip behavior of MgO are known [2.18–2.20]. MgO is highly ionic and slip occurs not on the close-packed {001} cubic planes but on the

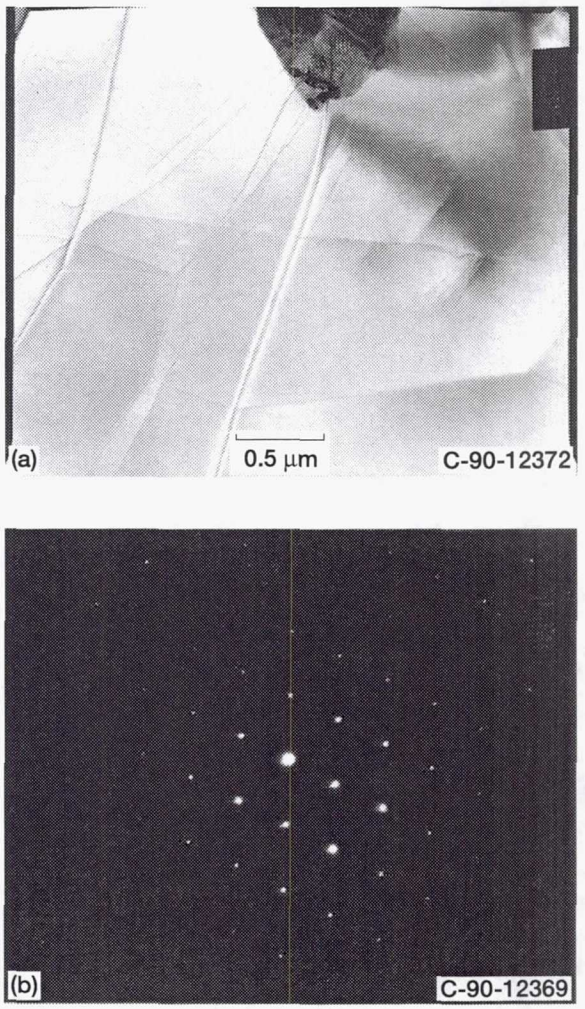

Figure 2.2.—Single-crystal molybdenite. (a) Transmission electron micrograph. (b) Transmission electron diffraction pattern.

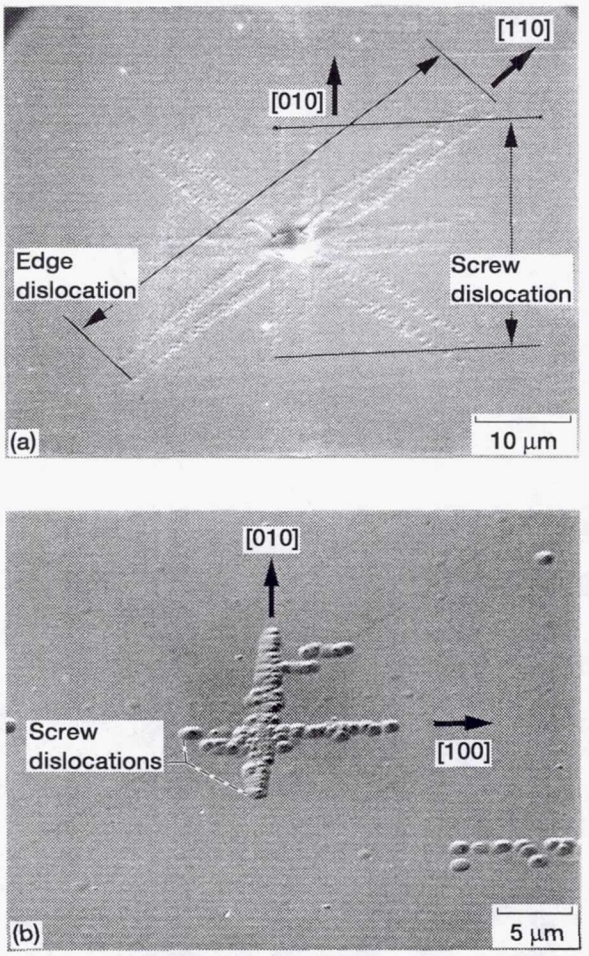

Figure 2.3.—Scanning electron micrographs showing distribution of dislocation etch pits on {001} magnesium oxide surface. (a) Around Vickers indentation made by diamond indenter at load of 0.1 N. (b) After exposure to cavitation for 10 s at 20 kHz (double amplitude, 50 mm) with 2 mm between vibrating disk and specimen in distilled water.

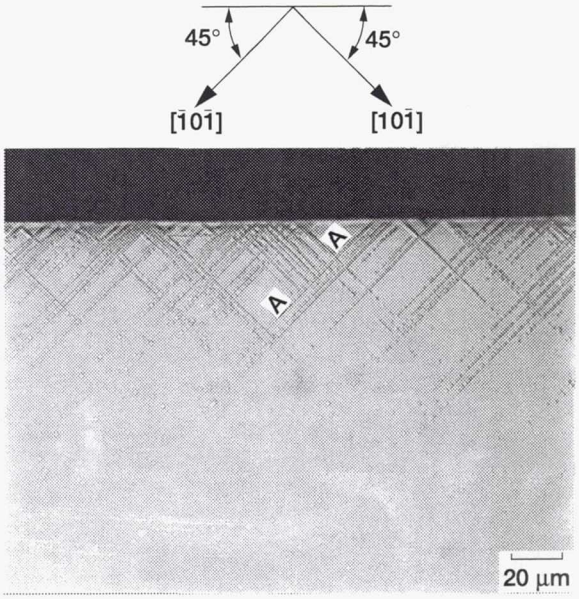

Figure 2.4.—Optical micrograph of dislocation-etch-pit patterns in cross section of MgO {001} surface after exposure to cavitation.

{011} cubic diagonals. MgO has six easy-slip planes, as shown in Fig. 2.5. In Fig. 2.5(a) two sets of {110} planes intersect the top surface at 45° (to be referred to as $\{110\}_{45°}$ planes). The dislocation lines on these planes that emerge on the top surface are screw dislocations because they lie parallel to their glide directions. In Fig. 2.5(b) the {110} planes intersect the top surface at 90° (to be referred to as $\{110\}_{90°}$ planes). The dislocation lines on these planes lie perpendicular to their glide directions and therefore are edge dislocations.

Figure 2.6 shows the length of the dislocation rows and the length of the diagonal of indentation as functions of load on a log-log scale. As expected, the gradient of the diagonal length is approximately 0.5 because the Vickers hardness is independent of indentation load. Almost the same gradient is shown for the length of edge dislocations. However, the gradient for the screw dislocations is slightly smaller, possibly because cross slips occur easily at higher loads. The row of edge dislocations is always longer than that of screw dislocations for the hardness indentations.

Figure 2.7 shows dark-field optical micrographs of the {001} surface after exposure to cavitation for 10 to 180 s. The specimen surface exposed for 10 s (Fig. 2.7(b)) has a number of cross-shaped damage areas with independent nuclei. The specimen surface exposed for 30 s (Fig. 2.7(c)) has both more and larger cross-shaped deformations (see a newly formed deformation at point A and

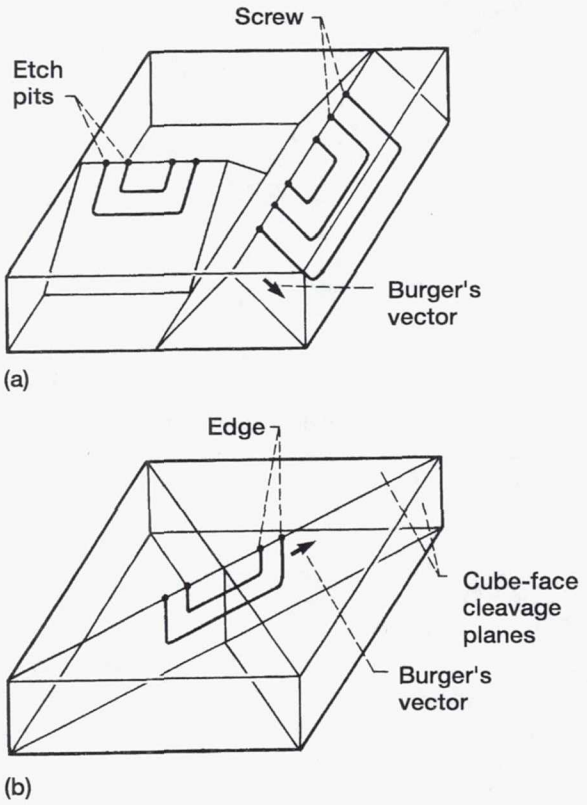

Figure 2.5.—Slip systems of MgO single crystal. (a) $\{110\}_{45^\circ}$ slip planes. (b) $\{110\}_{90^\circ}$ slip planes.

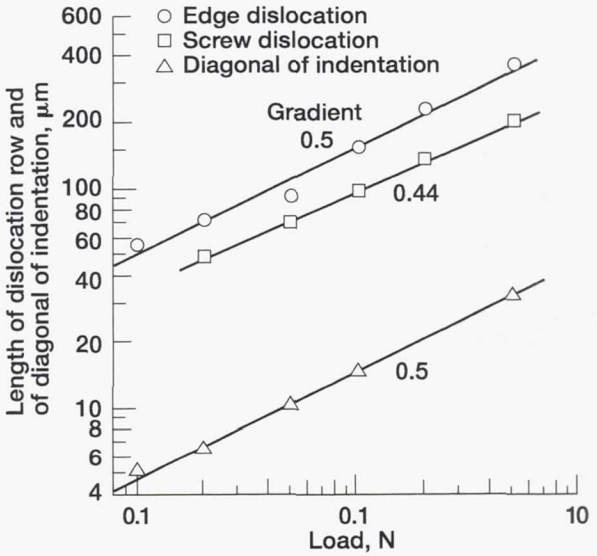

Figure 2.6.—Lengths of dislocation row and diagonal of indentation as function of load.

a large deformation at point B). The specimen surfaces exposed to cavitation for 60 and 180 s (Figs. 2.7(d) and (e), respectively) are fully covered with large cross-shaped deformations. The deformation pattern for 180 s is especially netlike, with wide dislocation rows. Thus, deformation damage along a preferred orientation accumulates with increased exposure time.

Indentation hardness anisotropy.—As hardness is a conventionally used parameter for indicating the abrasion resistance of tribomaterials, it is useful and important to consider the hardness anisotropy. Figure 2.8, as an example, shows a back-reflection Laue photograph and the results of Knoop hardness experiments made on the {0001} plane of single-crystal silicon carbide (SiC). The specimen is within ±2° of the low index {0001} plane. The Knoop hardness is presented as a function of the orientation of the long axis of the Knoop diamond indenter with respect to the $\langle 10\bar{1}0 \rangle$ direction at 10° intervals. The hardness decreases smoothly to a minimum value of about 2670 at a location near 30° from the $\langle 10\bar{1}0 \rangle$ direction. Figure 2.8 indicates that the $\langle 10\bar{1}0 \rangle$ direction is the maximum hardness direction and that the maximum hardness is about 2830. The hardness results are consistent with those of other workers [2.21, 2.22].

Friction anisotropy in abrasion.—If a hard material is brought into contact with a softer single crystal, the plastic deformation and accordingly the coefficient of friction of the single crystal are anisotropic and relate to the crystal structure. In crystals of comparable purity and crystallographic perfection, slip always begins when the shear stress across the slip planes reaches a certain definite value known

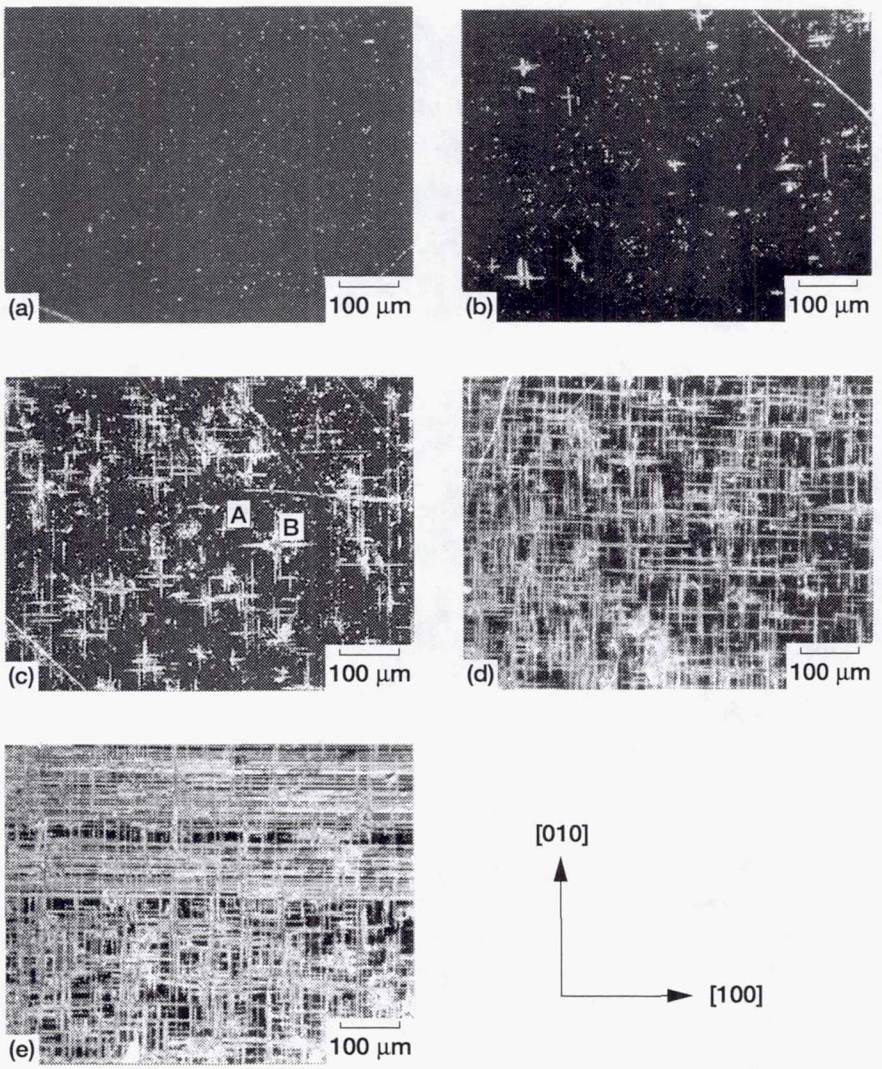

Figure 2.7.—Dark-field micrographs of dislocation-etch-pit patterns on {001} surface after exposure to cavitation. (a) New, cleaved surface. (b) After 10 s. (c) After 30 s. (d) After 60 s. (e) After 180 s.

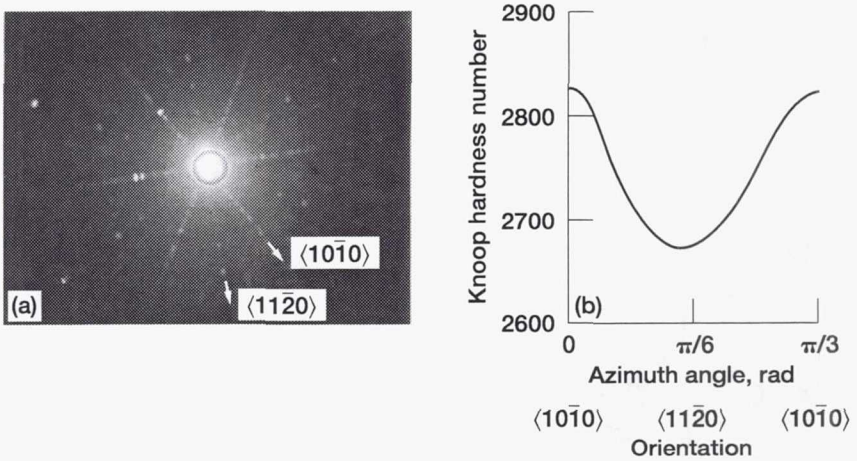

Figure 2.8.—Indentation hardness anisotropy of SiC {0001} basal plane. Measuring load, 2.9 N. (a) Back-reflection Laue photograph. (b) Knoop hardness as function of angle between long axis of Knoop indenter and ⟨10$\bar{1}$0⟩ direction axis.

as the critical resolved shear stress. The actual stress required to start deformation depends on the orientation of the slip planes relative to the applied stress. If the crystal is plowed or cut by a force F as in Fig. 2.9, the resolved stress on the slip plane in the slip direction is

$$\sigma = \frac{F}{A}\cos\phi\cos\lambda \tag{2.1}$$

where A is the projected area of contact and $\cos\phi\cos\lambda$ is the Schmid factor [2.23, 2.24]. The Schmid factor m is determined by the angles that the direction of the applied stress makes with the slip direction λ and with the normal to the slip plane ϕ. Therefore, the friction force F is

$$F = \frac{\sigma A}{m} \tag{2.2}$$

If the slip planes are nearly perpendicular to the sliding direction, ϕ approaches zero and a large force is required to initiate slip. This situation can arise in crystals of hexagonal-close-packed (hcp) metals and ceramics, such as zinc, magnesium, and Al_2O_3, where there is only one set of slip planes; in face-centered cubic (fcc) crystals there are four differently oriented sets of {111} slip planes so that, regardless of crystal axis orientation, there will be at least one set of slip planes more or less favorably oriented for slip.

When deformation occurs on a single set of parallel slip planes, it can continue until the crystal is literally sheared apart, with little stress increase above that

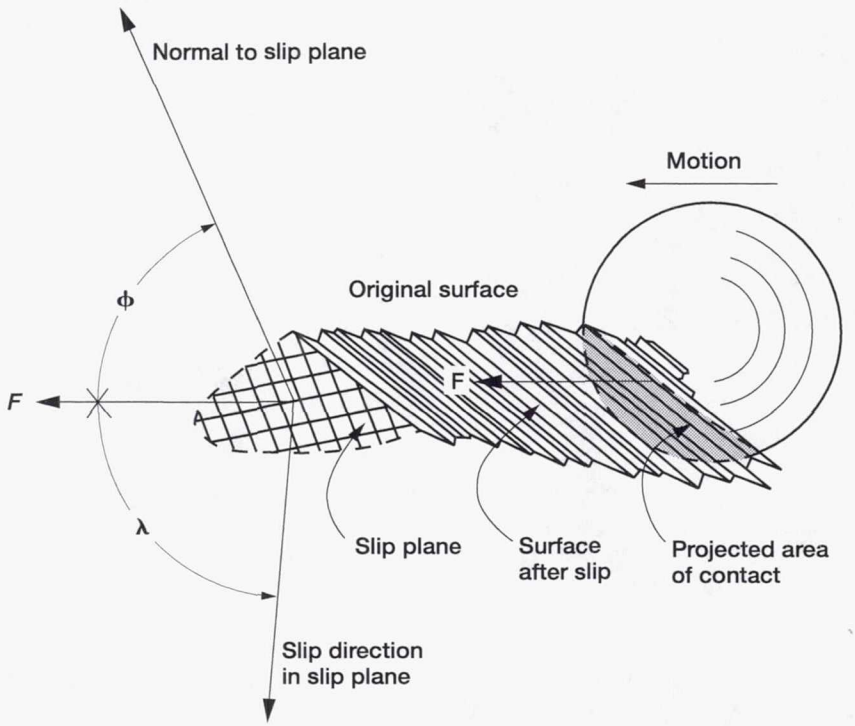

Figure 2.9.—Application of friction force to single crystal, causing slip to occur in definite direction. (The angle ϕ is measured between the normal to the slip plane and the axis of friction.)

needed to start deformation. If the crystal, as in the fcc case, has several sets of planes that can slip, then although deformation may begin on only one set, it will eventually start on others. The occurrence of slip on two or more sets of {111} planes means that active slip planes will interact with each other. This interaction hinders the glide on both sets, with the result that the stress must be continually increased to keep the deformation going. In single crystals of the hcp metals zinc and cadmium, the strain hardening—the rate of stress increase with strain—is small. In the fcc metals copper, aluminum, silver, and gold, it is much greater due to the intersecting slip systems.

As examples, anisotropic plastic deformation and fracture behavior of single-crystal ceramics in solid-state contact are discussed here as they relate to friction. Figures 2.10(a) and (b) show the coefficient of friction and the width of the permanent groove in plastic flow measured as functions of the crystallographic direction on the {0001}, $\{10\bar{1}0\}$, and $\{11\bar{2}0\}$ planes of single-crystal SiC in

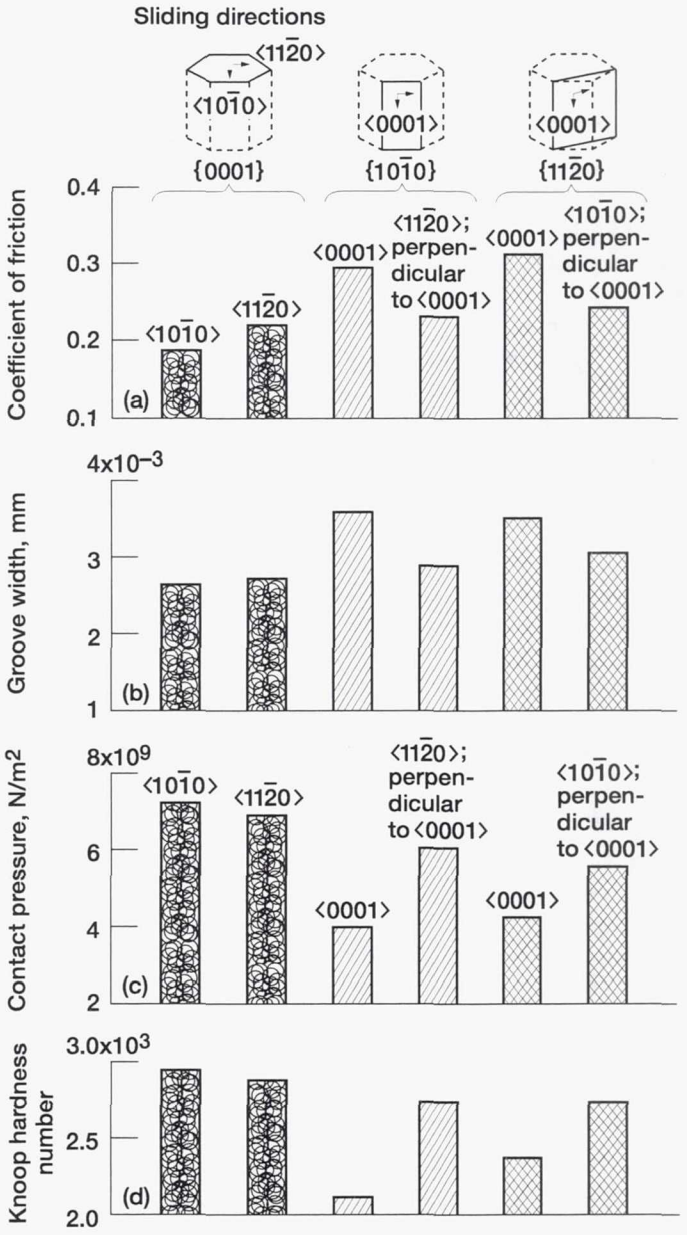

Figure 2.10.—Anisotropies on {0001}, {10$\bar{1}$0}, and {11$\bar{2}$0} SiC surfaces. (a) Coefficient of friction. (b) Groove width. (c) Contact pressure (load, 0.2 N). (d) Knoop hardness number (load, 1 N).

sliding contact with a spherical diamond pin in mineral oil. The results presented indicate that the coefficient of friction and the groove width are influenced by the crystallographic orientation. The $\langle 11\bar{2}0 \rangle$ direction on the basal $\{0001\}$ plane has the larger groove, primarily as a result of plastic flow, and is the direction of high friction for this plane. The $\langle 0001 \rangle$ directions on the $\{10\bar{1}0\}$ and $\{11\bar{2}0\}$ planes have the greater groove widths and are the directions of high friction when compared with the $\langle 11\bar{2}0 \rangle$ directions on the $\{10\bar{1}0\}$ plane and $\langle 10\bar{1}0 \rangle$ directions on the $\{11\bar{2}0\}$ plane. The anisotropies of friction are $\mu\langle 11\bar{2}0 \rangle / \mu\langle 10\bar{1}0 \rangle = 1.2$ on $\{0001\}$, $\mu\langle 0001 \rangle / \mu\langle 11\bar{2}0 \rangle = 1.3$ on $\{10\bar{1}0\}$, and $\mu\langle 0001 \rangle / \mu\langle 10\bar{1}0 \rangle = 1.3$ on $\{11\bar{2}0\}$.

Figure 2.10(c) represents the contact pressure calculated from the groove width data in Fig. 2.10(b) and the Knoop hardness obtained by other workers [2.21]. The anisotropy of the contact pressure during sliding and the Knoop hardness clearly correlate with each other.

The explanation for SiC slip behavior is known [2.25–2.28]. Several slip systems have been observed in hexagonal, single-crystal SiC, such as $\{0001\}\langle 11\bar{2}0 \rangle$, $\{3\bar{3}01\}\langle 11\bar{2}0 \rangle$, and $\{10\bar{1}0\}\langle 11\bar{2}0 \rangle$ [2.25, 2.26]. The $\{10\bar{1}0\}\langle 11\bar{2}0 \rangle$ slip system observed on the sliding surface was responsible for the anisotropic friction and plastic deformation behavior of SiC during sliding in the $\langle 10\bar{1}0 \rangle$ and $\langle 11\bar{2}0 \rangle$ directions on the SiC $\{0001\}$ surface. The experimental results on the $\{0001\}$ plane generally agreed with Daniels and Dunn's [2.27] resolved shear stress analysis based on the slip system $\{10\bar{1}0\}\langle 11\bar{2}0 \rangle$. The minima and maxima of the resolved shear stress for the $\{0001\}$ plane of a hexagonal crystal match the hard and soft directions on that plane (i.e., the $\langle 10\bar{1}0 \rangle$ and $\langle 11\bar{2}0 \rangle$ directions, respectively). The results shown in Fig. 2.10 cannot be explained by the resolved shear stress analysis based on the $\{0001\}\langle 11\bar{2}0 \rangle$ slip system [2.26]. Thus, the anisotropies of friction, contact pressure, and Knoop hardness on the $\{0001\}$ plane strongly correlate with the resolved shear stress based on the slip system $\{10\bar{1}0\}\langle 11\bar{2}0 \rangle$.

The anisotropies of friction, contact pressure, and Knoop hardness on the $\{10\bar{1}0\}$ and $\{11\bar{2}0\}$ planes correlate with the resolved shear stress [2.28] based on the $\{10\bar{1}0\}\langle 0001 \rangle$ and $\{10\bar{1}0\}\langle 11\bar{2}0 \rangle$ slip systems. They also correlate with the resolved shear stress [2.26] based on the $\{11\bar{2}0\}\langle 10\bar{1}0 \rangle$ slip system. However, the slip system actually observed in hexagonal SiC, the $\{10\bar{1}0\}\langle 11\bar{2}0 \rangle$ slip system, may be responsible for those anisotropies on the $\{10\bar{1}0\}$ and $\{11\bar{2}0\}$ planes.

Similar data for the Knoop hardness anisotropy of the tungsten carbide $\{0001\}$ and $\{10\bar{1}0\}$ surfaces have been reported by other workers [2.28], who used a resolved shear stress calculation involving the $\{10\bar{1}0\}\langle 0001 \rangle$ and $\{10\bar{1}0\}\langle 11\bar{2}0 \rangle$ slip systems to explain the data. Note that Fig. 2.10 suggests that the $\langle 10\bar{1}0 \rangle$ directions on the SiC basal plane would exhibit the lowest coefficient of friction and greatest resistance to abrasion resulting from plastic deformation.

Polycrystalline Materials

Both the weakest and strongest forms of metals such as iron are single crystals. In large single crystals the dislocations move easily; in microscopic whiskers the dislocations are immobile or perhaps absent. Extensive slip occurs more easily in single crystals than in polycrystalline materials with random grain orientations.

Important defects in polycrystalline materials are grain boundaries, or the interfaces between single-crystal grains. The boundaries are high-energy sites where they emerge on a solid surface, and they generally contain or act as an irregularity in the surface geometry because a cusp usually forms where the two grains meet. Grain boundaries are an atomic scale defect.

Slip will be blocked at every grain boundary in polycrystalline form; accordingly much greater stresses are required to deform a polycrystalline material, and much less deformation can be achieved before failure. A wide variety of materials, such as metals and ceramics, can be strengthened by decreasing the grain size (i.e., decreasing the mean free path for movement of dislocations). In a pure material the yield strength S is greatly increased by the presence of grain boundaries; this relationship can be derived from the Hall-Petch equation $S=S_i+k/d^{1/2}$, where d is the grain diameter and S_i and k are constants [2.23]. In solid solutions, solute segregation at the grain boundaries can further exaggerate the peculiarities of the regions. For example, a pronounced hardness peak occurs near grain boundaries in some solid solutions, such as a dilute solution of MgO in Al_2O_3. An important exception to the Hall-Petch relation occurs in certain high-strength materials at high temperatures (e.g., in MgO and in complex high-temperature alloys). In these materials deformation in the grain boundaries may become a major component of the deformation process; rupture strength then increases with increasing grain size and may be a maximum for a single crystal of the matrix phase.

2.2.2 Worked Layer

Mechanically abraded or polished metal, polymer, and ceramic surfaces are frequently used as lubricating coatings, self-lubricating substances, or wear-resistant substances. Such a surface is extremely rough on an atomic scale, and crystalline structure is distorted.

When a number of grits of hard abrasive material embedded in a resin matrix come into contact with a softer ceramic, the abrasive grits begin to cut or skive grooves in the ceramic surfaces (the so-called two-body condition). When abrasive-impregnated tapes rub on manganese-zinc (Mn-Zn) ferrite oxide ceramic ($MnO–ZnO–Fe_2O_3$), for example, the abrasive grits (e.g., SiC and Al_2O_3) can cut into and remove material from the oxide ceramic. Grooves are formed plastically primarily by the plowing and microcutting of the abrasive grits. Figure 2.11(a) presents a surface abraded in this manner [2.29]. A large number of plastically deformed grooves formed on the ferrite surface in the sliding direction of the

14-μm Al_2O_3 abrasive-impregnated tape. The maximum height of irregularities on the wear surface as measured by surface profilometer was 0.2 mm.

Figure 2.11(b) presents a scanning electron micrograph of the surface of a tape impregnated with 14-μm Al_2O_3 abrasive after 10 passes in sliding contact with Mn-Zn ferrite. Particles of Al_2O_3 are held in the nonmetallic binder. Figure 2.11(b) clearly indicates that relatively few abrasive grits were in contact with the ferrite and that ferrite was removed by a microcutting and plowing action. Only the tips of such grits contained ferrite wear debris particles involved in the abrasive action. Most of the ferrite debris observed on the tape surface was powdery and irregular in shape, but some was curled, indicating a cutting action.

When a third particle harder than one or both of the surfaces in contact becomes trapped at the interface, abrasive wear, lapping, or polishing can also occur, removing material from one or both surfaces. This mode of wear is called three-body abrasion. For example, Fig. 2.12 presents replication electron micrographs and reflection electron diffraction patterns of single-crystal Mn-Zn ferrite wear surfaces abraded by 15- and 4-μm SiC grits in the three-body condition. The abrasion with 15-μm SiC grits resulted in brittle fractured facets on the Mn-Zn ferrite surface due to cleavage and quasi-cleavage. The 4-μm SiC grits mostly produced a large number of plastically deformed indentations and grooves, formed primarily by plowing and microcutting, as well as a few brittle fractured facets.

Reflection electron diffraction patterns taken on both abraded single-crystal Mn-Zn ferrite surfaces (Fig. 2.12) contain continuous arcs extending over nearly a semicircle that indicate a surface in a polycrystalline state. The rest were blocked out by the shadow of the solid specimen. The arcs for the abraded surface generated by the 4-μm SiC grits are much broader than those for the abraded surface generated by the 15-μm SiC grits. The broad arcs indicate the large extent of plastic deformation on the abraded surface generated by the 4-μm SiC grits. Thus, the abrasion mechanism for Mn-Zn ferrite oxide ceramics is drastically changed by the size of the abrasive grits. With 15-μm SiC grits ferrite abrasion is principally due to brittle fracture, whereas with 4-μm SiC grits it is due to plastic deformation.

The plastic deformation and microcracks subdivide a single-crystal Mn-Zn ferrite into polygonal subgrains, as described above. The nature of the strain or structural surface damage varies with depth from the surface. This variation can be revealed by combining chemical etching with reflection electron diffraction. For example, Fig. 2.13 shows a replication electron micrograph of an abraded single-crystal Mn-Zn ferrite {110} surface, similar to that in Fig. 2.11(a), and reflection electron diffraction patterns of the surface after chemical etching. The diffraction patterns indicate a surface severely distorted and in a highly textured polycrystalline state ranging from textured to nearly amorphous. The diffraction pattern from the ferrite surface etched to a depth of 0.2 μm (Fig. 2.14(a)) shows a large streak-spot pattern. The streaking indicates severe plastic deformation (i.e., a highly strained, mosaic, single-crystal structure). Large numbers of line defects can cause

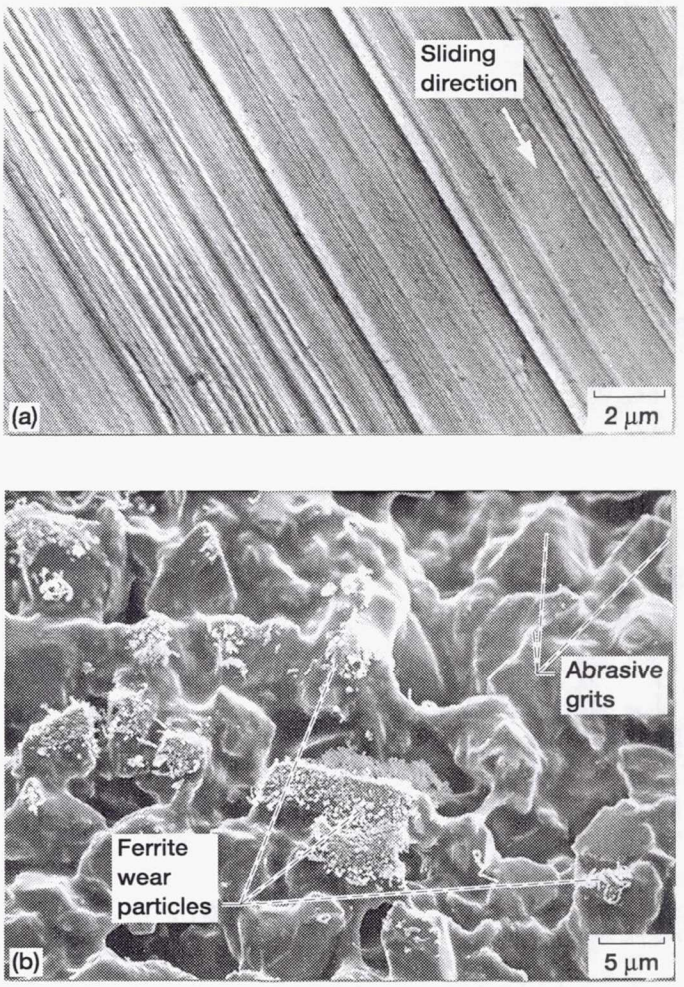

Figure 2.11.— Wear surfaces. (a) Replication electron micrograph of Mn-Zn ferrite surface after single-pass sliding of tape impregnated with 14-μm Al_2O_3 (sliding surface, {110}; sliding direction, ⟨110⟩; sliding velocity, 11.19 m/s; laboratory air; room temperature). (b) Scanning electron micrograph of tape impregnated with 14-μm Al_2O_3 after 10-pass sliding against Mn-Zn ferrite (sliding velocity, 0.52 m/s; laboratory air; room temperature).

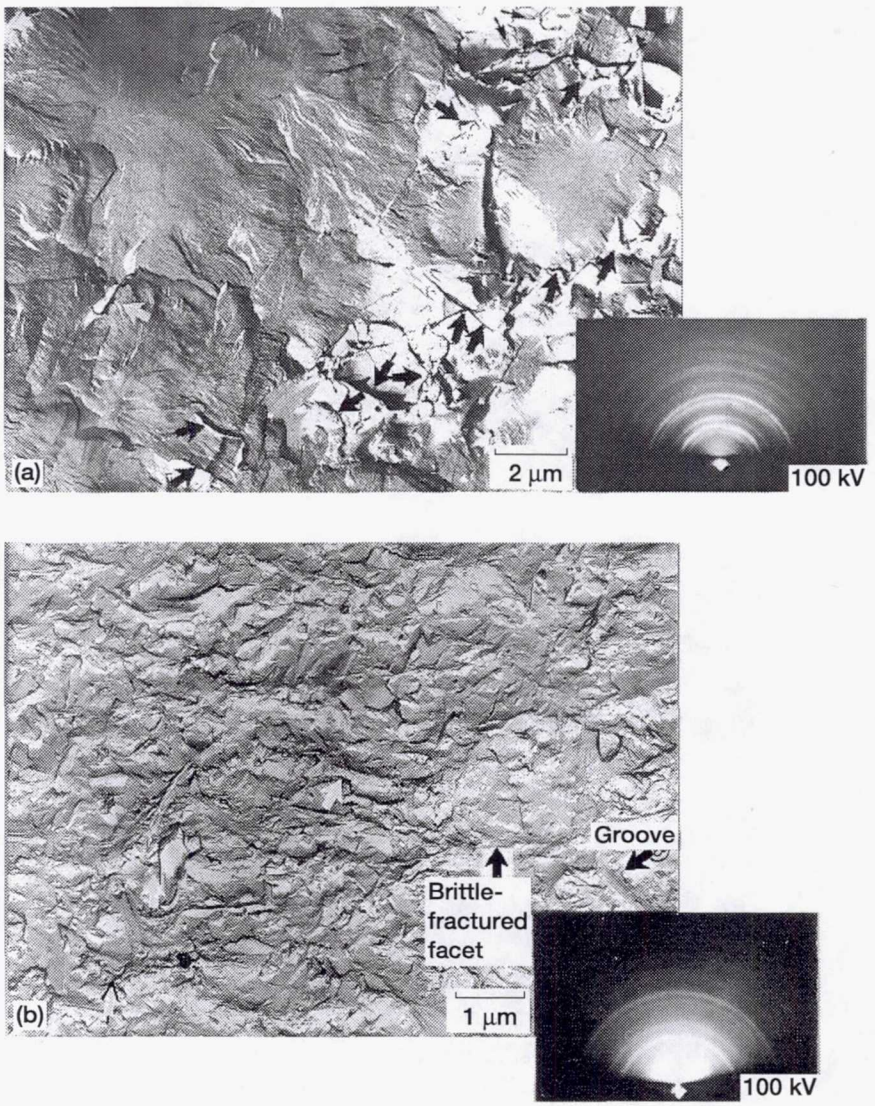

Figure 2.12.—Replication electron micrographs and reflection electron diffraction patterns of abraded single-crystal Mn-Zn ferrite {110} surface. Abrasion direction, ⟨011⟩; lapping disk, cast iron; lapping fluid, olive oil; sliding velocity, 0.5 m/s; abrasive-to-fluid ratio, 27 wt%. (Arrows denote cracks.) (a) After contact with 15-μm SiC grit at 3 N/cm^2. (b) After contact with 4-μm SiC grit at 8 N/cm^2.

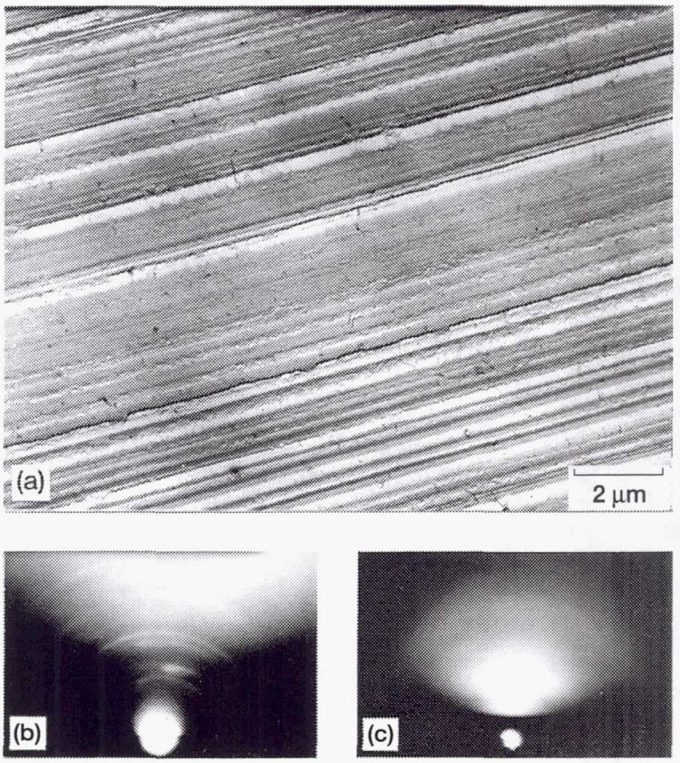

Figure 2.13.—Mn-Zn ferrite {110} surface after sliding on Al_2O_3 lapping tape (1000 mesh). (a) Replication electron micrograph. Electron diffraction patterns showing (b) highly textured polycrystalline surface and (c) nearly amorphous surface.

streaking in a diffraction pattern. Strain and structural damage decrease at greater depths below the abraded surface. At 0.4 μm below the surface (Fig. 2.14(b)) the diffraction pattern shows a relatively sharp spot pattern and no streaking. At depths of 0.8 and 1.0 μm (Figs. 2.14(c) and (d)) the patterns show Kikuchi lines (pairs of black and white lines), which indicate a bulk crystalline structure containing no mechanically stressed areas. Thus, reflection electron diffraction studies can reveal the type of surface damage as well as the total thickness of the deformed, worked layer.

Figure 2.15 schematically summarizes the crystal structure of the worked layer verified by reflection electron diffraction and chemical etching techniques. It also presents the etching rate for the abraded surface as a function of etching depth (distance from the abraded surface). This graph is called an etching rate–depth profile. The outermost layer, which is textured and polycrystalline, has the highest

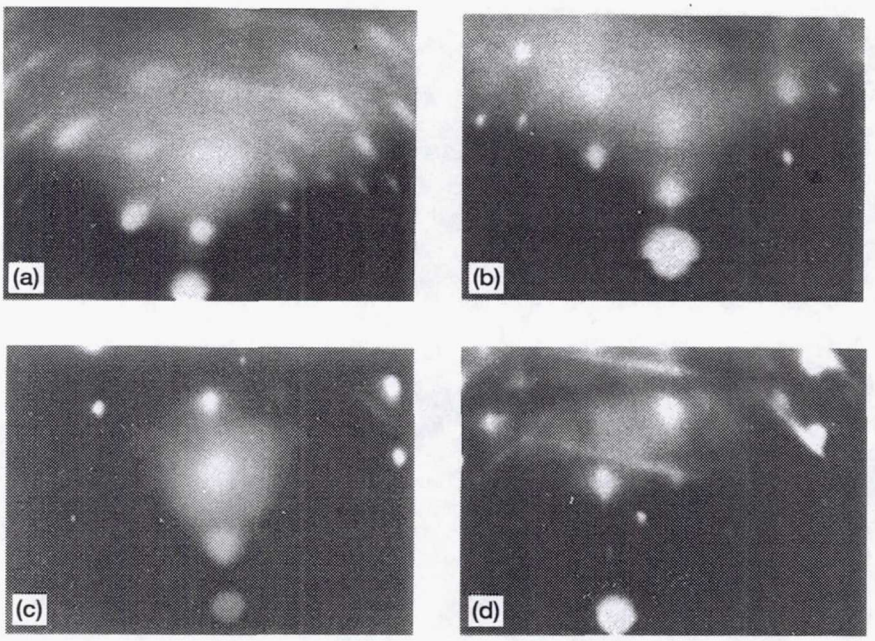

Figure 2.14.—Reflection electron diffraction patterns of etched surfaces of surface in Fig. 2.13(a) at etching depths of (a) 0.2 μm, (b) 0.4 μm, (c) 0.8 μm, and (d) 1 μm.

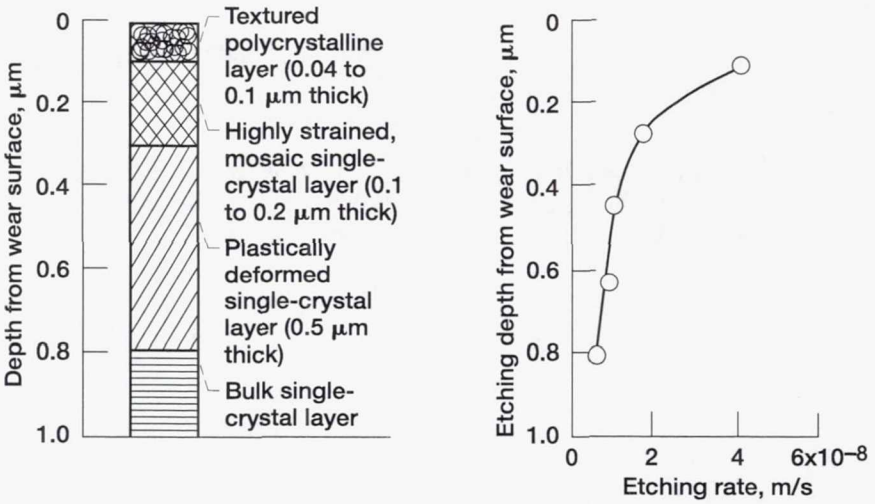

Figure 2.15.—Crystal structure of deformed layer and etching rate as function of etching depth. (Sliding materials same as in Fig. 2.13.)

etching rate, indicating that the layer contains severe defects. A decreasing etching rate is related to decreasing defects: the fewer the defects, the lower the etching rate.

The thickness of the worked layer and the degree of deformation in the layer are functions of (1) the amount of work, or energy, put into the deformation process and (2) the structure and composition of the solid. Figure 2.16(a) shows that the worked layer thickened as the normal load increased. Note that at all loads the greater part of the worked layer was composed of a plastically deformed single-crystal layer (Fig. 2.16(b)), which increased in extent as the load increased. The etching rate (Fig. 2.16(c)) also depended on the normal load applied during abrasion; that is, the number of defects in the worked layer increased with increasing normal load. Some solids are much more prone to deformation than are others. This, of course, would be reflected in these surface layers.

Worked layers are extremely important in tribology and in solid-film lubricant deposition because their physical, chemical, and mechanical properties can be entirely different from those in the bulk solid. Further, these properties depend on the depth of the worked layers and on the concentration and nature of the defects, such as whether they are dislocations or microcracks. For example, extrinsic magnetic properties of Mn-Zn ferrites, such as initial permeability, coercive force, and magnetic loss, are influenced by both the surface and bulk crystalline states of the ferrite. On a videotape recorder the sliding of the magnetic tape abrades the ferrite head and scratches its surface. Considerable plastic flow occurs on the ferrite surface, and the large number of defects produced can drastically change the crystalline state of the ferrite head and produce a worked layer on its surface. The worked layer decreases readback signal amplitude and degrades the signal obtained in short-wavelength recording. Figure 2.17(a) shows the readback signals from a new, chemically etched Mn-Zn ferrite magnetic head in sliding contact with a magnetic tape as a function of sliding distance. Figures 2.17(b) and (c) show the electron diffraction patterns taken from the magnetic head surface before and after the sliding. Clearly, the sliding action changed the crystalline state of the magnetic head surficial layer from a single-crystal structure to a nearly amorphous one. That crystallographic change in Mn-Zn ferrite is a critical factor in the readback signal losses shown in Fig. 2.17(a).

2.2.3 Surface Roughness and Topography

All surfaces contain irregularities, or hills and valleys. Even in cleaved surfaces of single-crystal materials there are cleavage steps. Surface topography is a permanent record of the deformation and fracture process and provides valuable information on surface properties. The world of the engineer is made of solids whose surfaces acquire their texture from many processes, such as cutting, grinding, lapping, polishing, etching, peening, sawing, casting, molding, calendering, and coating [2.30]. Surface topography, or roughness, is an important parameter in characterizing engineering surfaces used in tribological applications.

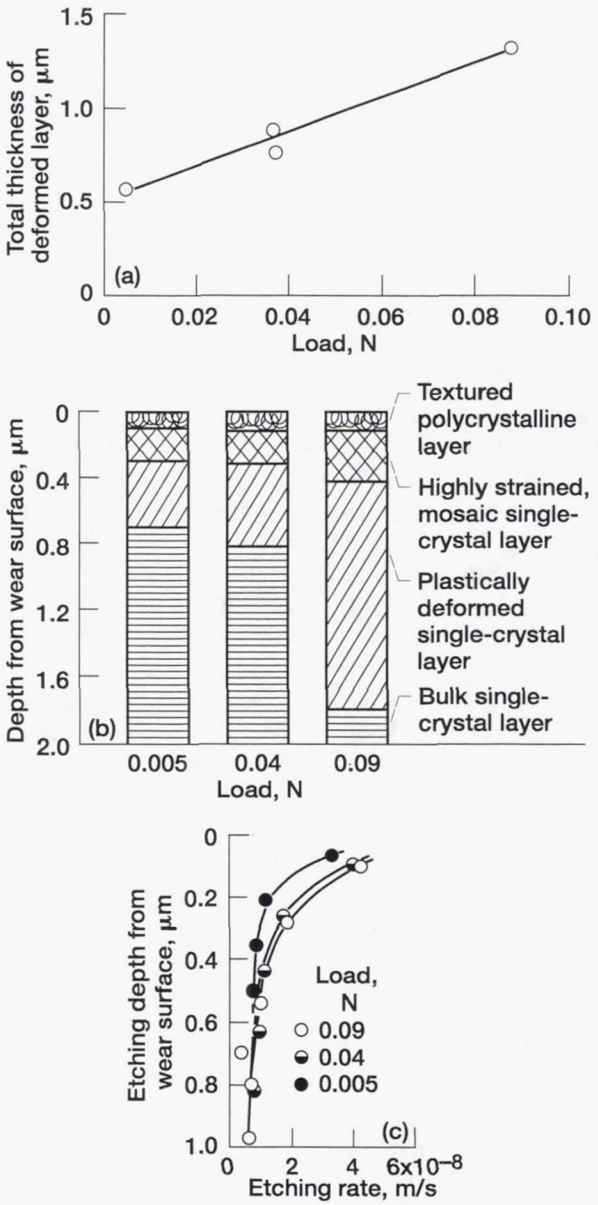

Figure 2.16.—Crystal structure of deformed layer as function of load. (Sliding materials same as in Fig. 2.13.) (a) Layer thickness as function of load. (b) Depth from wear surface as function of load. (c) Etching rate as function of etching depth.

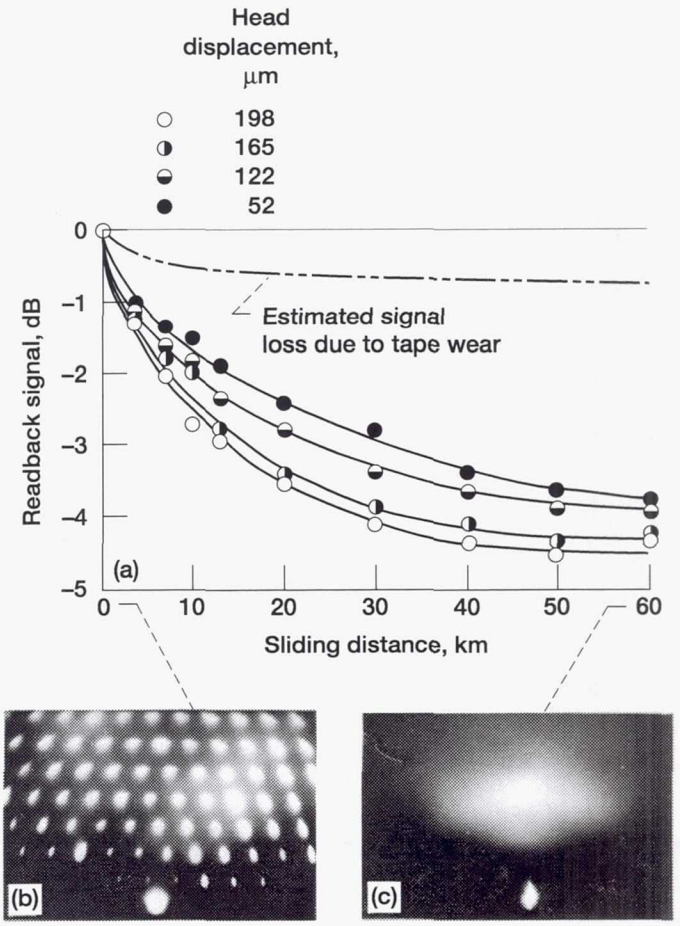

Figure 2.17.—Crystal structure and magnetic signal as function of sliding distance. Sliding materials, chemically etched Mn-Zn ferrite and magnetic tape. (a) Readback signal. Electron diffraction patterns of (b) highly strained single-crystal structure before sliding and (c) nearly amorphous structure after 60 km of sliding.

The unaided eye, fingers, hand lens, optical microscope, optical (interferometry) profiler, stereo microscope, scanning electron microscope, transmission electron microscope with replicas (sometimes also used in optical microscopy), stylus profilometer, and scanning probe microscopes (e.g., scanning tunneling microscope and atomic force microscope) are typically used for studying surface topography [2.31]. Gross features, such as tool marks, isotropy of the surface texture, surface defects, and discoloration, are often best viewed with the unaided eye. Such viewing is rapid and versatile, allows large areas to be examined, and generally prevents details from obscuring the overall pattern. Also, surface texture and roughness are virtually felt with the fingers as they touch a solid surface. The hand lens (e.g., 10X) extends the eye's capability without much loss of speed or surface inspection area. The optical microscope remains one of the most useful and cost-effective tools, in terms of initial cost as well as speed, effectiveness, and versatility of use.

The optical (interferometry) profiler can measure surface features without contact. Light reflected from the surface of interest interferes with light from an optically flat reference surface. Deviations in the fringe pattern produced by the interference are related to differences in surface height. If an imaging array is used, three-dimensional information can be provided. In general, optical profilers have some advantages—no specimen preparation and short analysis time—but also some disadvantages. If the surface is too rough (roughness greater than 1.5 μm), the interference fringes can be scattered to the extent that topography cannot be determined. If more than one matrix is involved (e.g., multiple thin films on a substrate, or if the specimen is partially or totally transparent to the wavelength of the measurement system), measurement errors can be introduced. Multiple-matrix specimens can be measured if coated with a layer that is not transparent to the wavelength of light used.

The stereo microscope allows for three-dimensional viewing of specimens themselves, of a stereogram, or of a pair of stereo pictures taken by an optical or scanning electron microscope. Stereo imaging consists of two images taken at different angles of incidence a few degrees apart. Stereo imaging, in conjunction with computerized frame storage and image processing, can provide three-dimensional images with the quality normally ascribed to optical microscopy.

The scanning electron microscope produces micrographs with sufficient resolution to reveal individual features (lateral resolution of 1 to 50 μm in the secondary electron mode at sampling depths from a few nanometers to a few micrometers, depending on the accelerating voltage and the analysis mode) and yet with a large enough field of view that the interrelation of many such features can be seen. In practice, however, the scanning electron microscope has three disadvantages: specimen size is limited to 10 cm or smaller, roughness cannot be quantified, and specimens must be vacuum compatible [2.30, 2.31]. Surface features can be measured best by cleaving the specimen and taking a cross-sectional view.

Transmission electron microscopy is always of replicas (sometimes also used in optical microscopy). It delineates surface features, such as fine pores, cracks, grooves, and especially cleavage steps, better than scanning electron microscopy (e.g., see Fig. 2.12). The transmission electron microscope has some disadvantages: the difficulty of locating specific areas limits it to general characterization and large features, such as large pores, and it fails to reveal cracks owing to replica breakage at these points.

The stylus profilometer (mechanical profilometer) is today most widely used for measuring surface roughness and analyzing surface topography. A diamond stylus with a tip radius of a few micrometers moves up and down as it is dragged across a specimen surface. This up-and-down motion effectively replicates the surface topography. Lateral resolution depends on the stylus radius. If the radius of curvature of the surface of interest is smaller than the radius of curvature of the stylus, the measurement will not satisfactorily reproduce the surface. The typical stylus radius is about 3 μm, but smaller radii down to submicrometer sizes are available. The load applied to the stylus is usually in the millinewton range, 1 to 40 mN. In spite of the light loads used, however, the contact pressure is on the order of gigapascals and is sufficiently large to damage surfaces. Sampling distance ranges from tens of micrometers to tens of millimeters. No specimen preparation is required, almost any specimen regardless of engineering material can be measured rapidly, and results can be obtained in seconds. The stylus profiler provides somewhat limited two-dimensional information. For three-dimensional topographical information, consecutive line scans are needed. This procedure can be quite time consuming.

Scanning probe microscopes [2.31, 2.32] can be considered as derivatives of the stylus profilometer. One popular variant is the scanning tunneling microscope (STM). In this technique a tip is brought to within one nanometer of the specimen surface, and a small bias voltage of typically 0.01 to 1 V is applied between them. Under these conditions electrons can penetrate the potential barrier between a specimen and a probe tip, producing an electron tunneling current I that varies exponentially with tip-to-surface spacing s as follows:

$$I \propto e^{-1.025\sqrt{\varphi}s} \tag{2.3}$$

where ϕ is the composite work function in electron volts (typically ~4 eV) and s is in angstroms (1 Å equals 0.1 nm). If the tip-to-surface spacing increases (or decreases) by 1 Å, the tunneling current decreases (or increases) by about a factor of 10. Therefore, the tunneling current is a sensitive function of tip-to-surface spacing s. The exponential dependence of the magnitude of I upon s means that, in most cases, a single atom on the tip will image the single nearest atom on the specimen surface. This tunneling current is the imaging mechanism for the scanning tunneling microscope. A piezoelectric scanner is usually used as an

extremely fine positioning stage to move the probe over the specimen (or the specimen under the probe).

Clearly, this technique works only with conducting and semiconducting materials. With insulating materials one can put on conducting coatings. Alternatively, one can use a different form of scanning probe microscope, namely, the atomic force microscope (AFM), also called a scanning force microscope (SFM).

An atomic force microscope, instead of using the electron tunneling current to measure the tip-to-surface distance, can measure the force of interaction between a specimen surface and a sharp probe tip. The tip, a couple of micrometers long and often less than 10 nm in diameter, is located at the free end of a cantilever 100 to 200 μm long. When the tip comes within a few angstroms of the specimen's surface, repulsive van der Waals forces between the atoms on the tip and those on the specimen cause the cantilever to deflect, or bend. Figure 2.18 shows the dependence of the van der Waals force on the tip-to-surface spacing. A detector, such as the position-sensitive photodetector (PSPD) measures the cantilever deflection as the tip is scanned over the specimen or the specimen is scanned under the tip (Fig. 2.19). As a piezoelectric scanner gently traces the tip across the specimen (or the specimen under the tip), the contact force causes the cantilever to bend to accommodate changes in topography. The measured cantilever

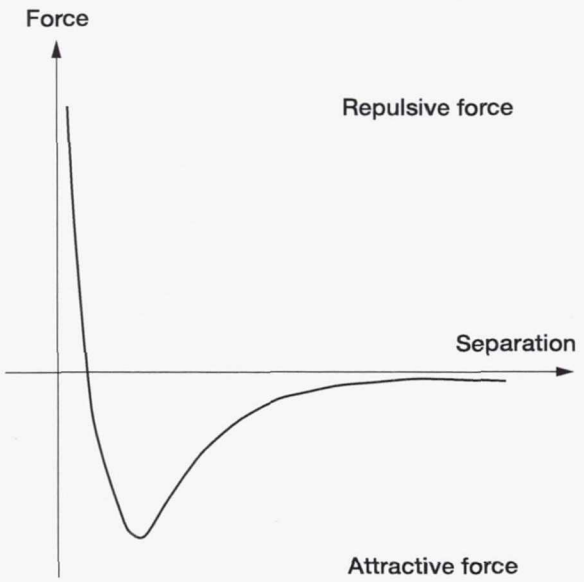

Figure 2.18.—Van der Waals force as function of tip-to-specimen separation. (Atomic force microscopes can be designed to operate in either of the two regimes indicated by the heavy lines.) (From [2.32].)

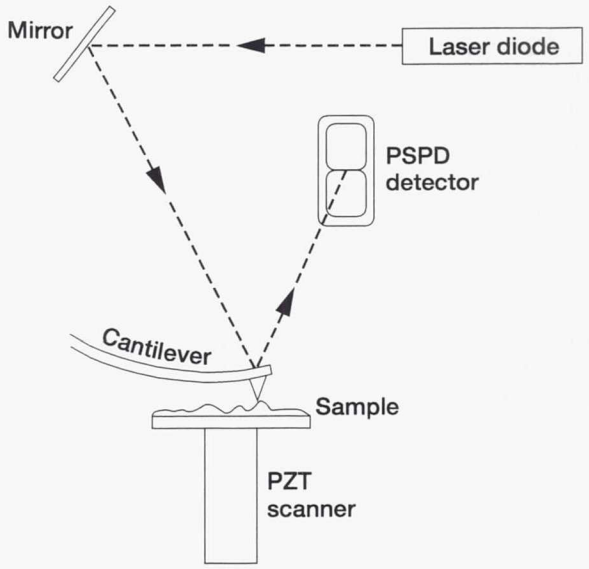

Figure 2.19.—Schematic diagram of optical technique for detecting cantilever deflection (also called bounce-beam detection). (From [2.32].)

deflections allow a computer to generate a map of surface topography. Atomic force microscopes can be used to study insulating and semiconducting materials as well as electrical conducting materials.

Note that in Fig. 2.18 at the right side of the curve the atoms are separated by a large distance. As the atoms are gradually brought together, they will first weakly attract each other. This attraction increases until the atoms are so close together that their electron clouds begin to repel each other electrostatically. This electrostatic repulsion progressively weakens the attractive force as the interatomic separation continues to decrease. The force goes to zero when the distance between the atoms reaches a couple of angstroms, about the length of a chemical bond. When the total van der Waals force becomes positive (repulsive), the atoms are in contact. The slope of the van der Waals curve is steep in the repulsive or contact region. As a result, the repulsive van der Waals force will balance almost any force that attempts to push the atoms closer together. In the atomic force microscope this means that when the cantilever pushes the tip against the specimen, the cantilever will bend rather than forcing the tip atoms closer to the specimen atoms.

Most atomic force microscopes currently used detect the position of the cantilever with optical techniques. In the most common scheme, shown in Fig. 2.19, a laser beam bounces off the back of the cantilever onto the position-sensitive

photodetector. As the cantilever bends, the position of the laser beam on the detector shifts. The position-sensitive photodetector itself can measure displacements of light as small as 1 nm. The ratio of the path length between cantilever and detector to the length of the cantilever itself produces a mechanical amplification. As a result, the system can detect even 0.1-nm vertical movement of the cantilever tip. Other methods of detecting cantilever deflection rely on optical interference, a scanning tunneling microscope tip, or piezoresistive detection (fabricating the cantilever from a piezoresistive material).

The shape of a surface can be displayed by a computer-generated map developed from digital data derived from many closely spaced parallel profiles taken by this process. Such a map shows details of individual features and also the general topography over an area and describes surfaces. Figures 2.20(a) and (b) are examples of atomic force microscopy images of an ion-beam-deposited, diamondlike carbon film and a chemical-vapor-deposited, fine-grain diamond film on mirror-polished silicon substrates (DLC on silicon and CVD diamond on silicon). The surface of the diamondlike carbon film has a smooth, flat morphology. The CVD diamond surface has a granulated or spherulitic morphology: the surface contains spherical asperities of different sizes. The surface roughness of the DLC on silicon is 0.49 nm root-mean square (rms); the surface roughness of the CVD diamond on silicon is 58.8 nm rms. Also, Fig. 2.20 shows actual height profiles, histograms, and bearing ratios for the DLC on silicon and the CVD diamond on silicon. Height profiles, histograms, and bearing ratios are explained in the following paragraphs.

The fraction of a surface lying in each stratum can readily be obtained by sampling its height at regular intervals or by tracing a profile. This procedure gives the height profile (distribution curve of roughness), bearing ratio (Abbott's bearing curve) or bearing area curve, height histogram, and height distribution, as shown in Fig. 2.21. Many engineering surfaces have height distributions that are approximately Gaussian (i.e., they can be described by the normal probability function)

$$f(u) = \frac{1}{\sqrt{2\pi}\sigma} e^{-(1/2)(u/\sigma)^2} \tag{2.4}$$

where u is a deviation from the median line of the profile curve and σ is the standard deviation of the profile curve.

It is also useful to describe surfaces in terms of the integral of the distribution (bearing ratio in Fig. 2.21(b)), which gives the fraction of the surface at or below each height. The well-known Abbott's bearing curve, which gives the contact area that would exist if the hills were worn down to the given height by an ideally flat body, is the fraction of the surface at or above each height. Some modern surface analyzers provide chart or video displays of height histogram and bearing ratio as standard features. Examples are shown in Fig. 2.20.

Profiles of engineering surfaces usually contain three major components: roughness, waviness, and errors of form, as shown in Fig. 2.22 [2.30, 2.33].

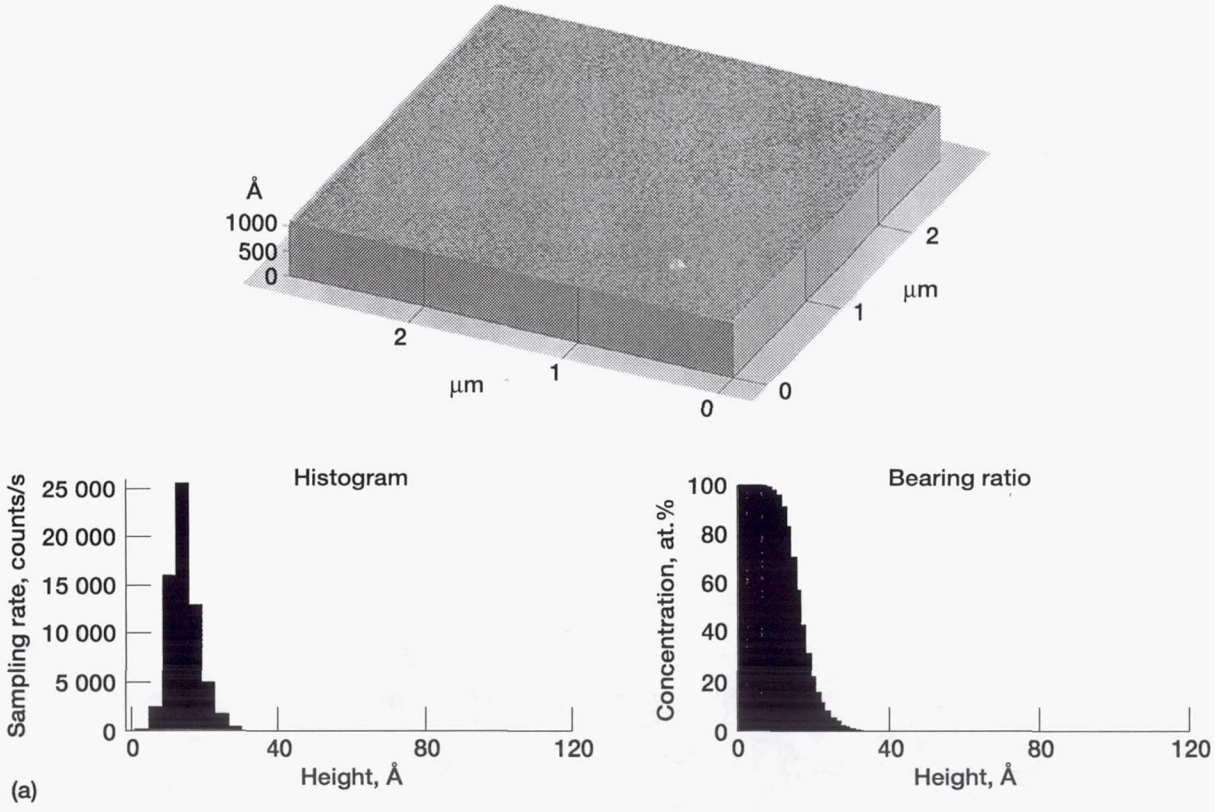

Figure 2.20.—Atomic force micrographs of diamond films on mirror-polished silicon substrates. (a) Ion-beam-deposited, diamondlike carbon film. (b) Chemical-vapor-deposited, fine-grain diamond film.

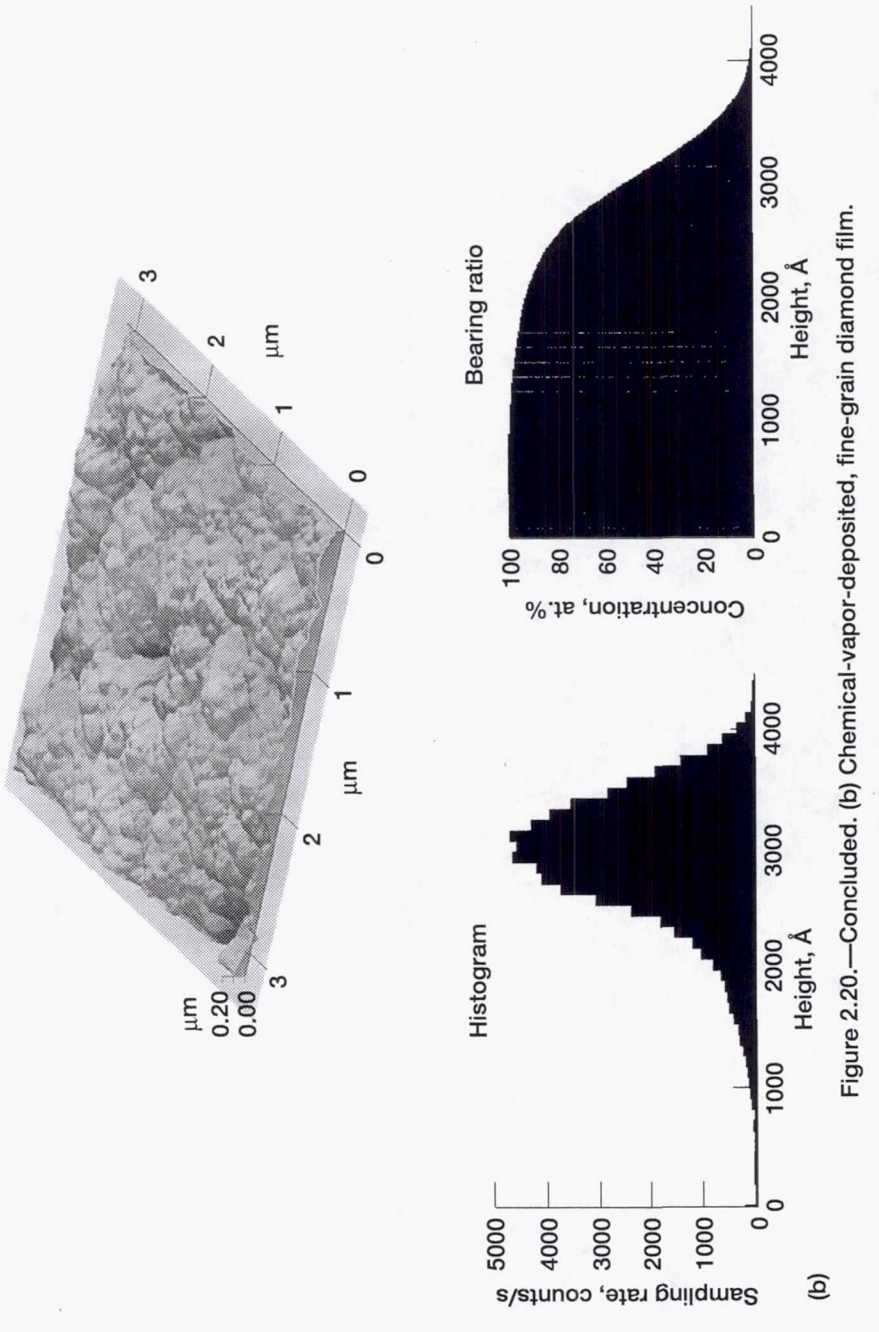

Figure 2.20.—Concluded. (b) Chemical-vapor-deposited, fine-grain diamond film.

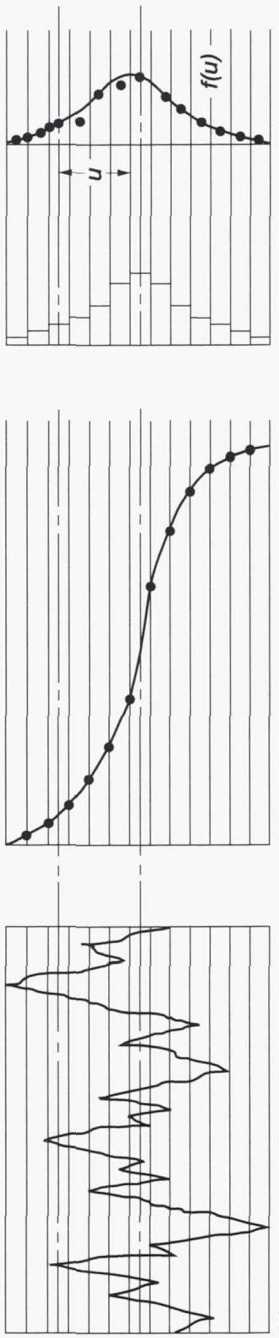

Figure 2.21.—Fraction of surface lying in each stratum. (a) Height profile (distribution curve of roughness). (b) Bearing ratio (Abbott's bearing curve) or bearing area curve. (c) Height histogram. (d) Height distribution.

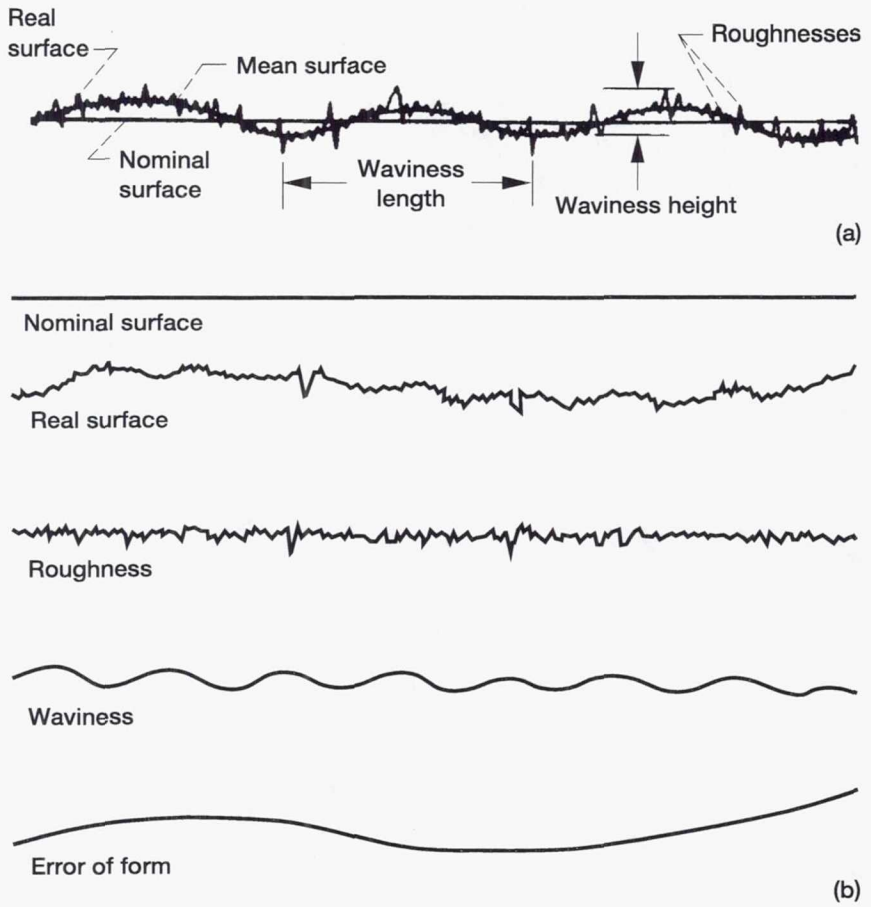

Figure 2.22.—Magnified surface profile (a) and its components (b). (From [2.30, 2.33].)

Roughness shows closely spaced irregularities, the height, width, and direction of which create the predominant surface pattern. Roughness includes those surface features intrinsic to the production process. Waviness shows surface irregularities of greater spacing than roughness. It is often the results of heat treatment, machine or workpiece or specimen deflections, vibrations, or warping strains. Errors of form are gross deviations from the nominal or ideal shape. They are not normally considered part of the surface texture.

Surface roughness occurs at all length scales. Figure 2.23 presents length scales for various surface-related phenomena of interest in engineering. The size range of contaminant particles in the environment is enormous. Such particles include human particles (hair, skin flakes), combustion products (smoke, fly ash), and particles produced by abrasion (machining, car tires, sand). In general, any

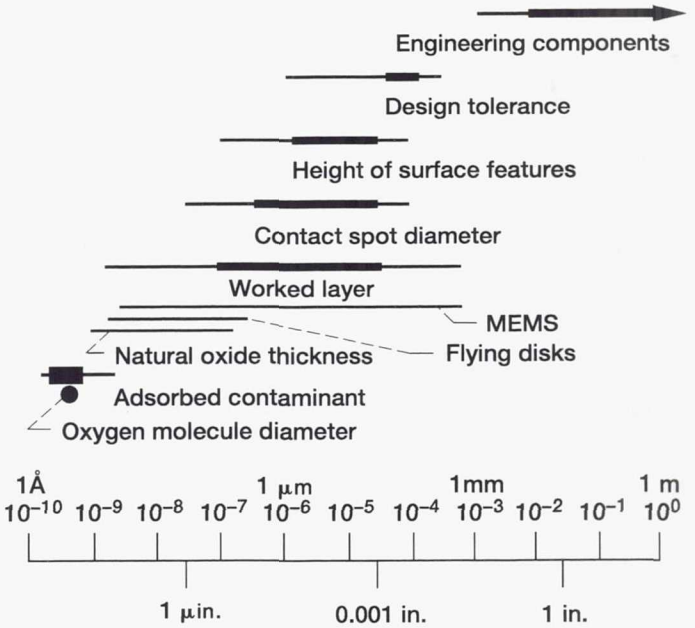

Figure 2.23.—Comparative size of surface-related phenomena. (From [2.30].)

system involving fluid bearings is susceptible to contaminant particle damage. The dimensions of microelectromechanical systems (MEMS) and the flying heights of magnetic hard disk drives range from tens of micrometers down to tens of nanometers. The scale of the world in tribology is essentially determined by the size of the contact areas between surfaces. The diameters of contact spots range from about 100 μm down to less than 1 μm, similar to the height range of surface features. The width of that range is large and so is the depth of the worked layers.

Let us now statistically consider the size of the contact areas between surfaces [2.34, 2.35]:

1. An ideal surface in contact with a rough surface
2. A rough surface in contact with a rough surface

When a hard, ideal flat surface is brought into contact with a soft, rough surface having the Gaussian height distribution, the actual contact takes place over a small area, actually at the tips of the asperities or surface irregularities, as indicated in Fig. 2.24(a). The distance $m\sigma$ between the ideal surface and the median line of the profile curve for the rough surface is the distance between the tips of the highest asperities and the median line of the profile curve. The constant m can be determined from the peak-to-valley profile height. These asperity regions initially deform elastically, and then, if the load is sufficiently high, they deform plastically until

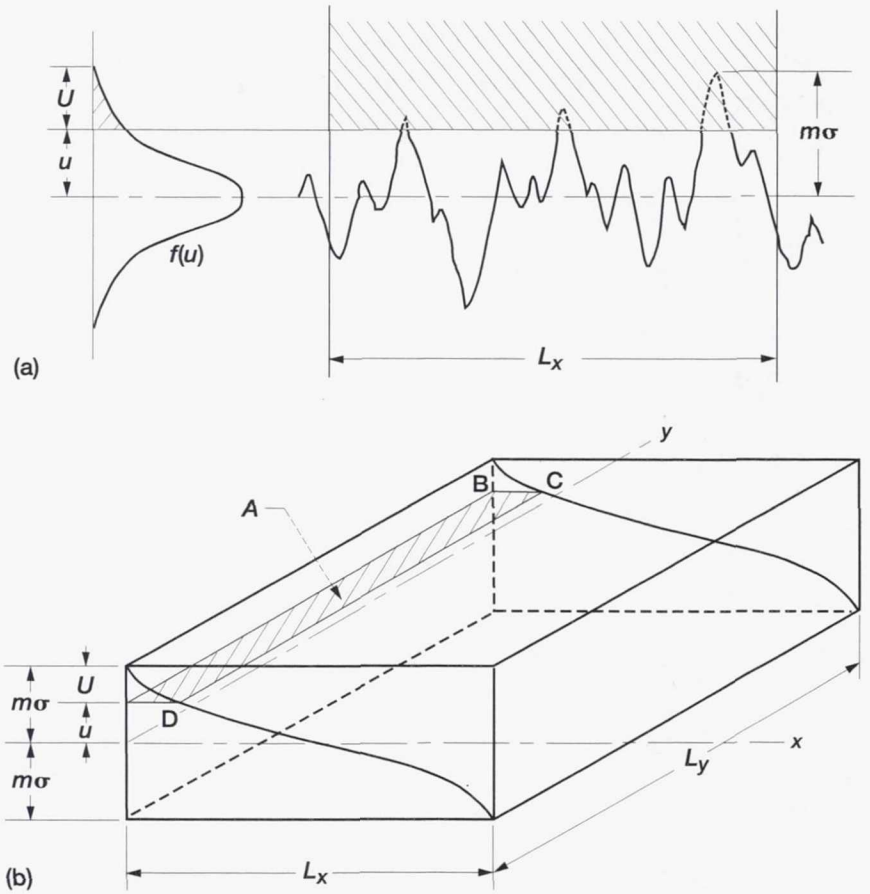

Figure 2.24.—Contact between ideal flat surface and rough surface (a), and Abbott's bearing curves on L_x and L_y and real area of contact A (b).

the load can be supported. That is, the real contact area A continues to increase with deformation until it is sufficient to support the load W applied to the two surfaces in solid-state contact. In this case, A may be approximated by

$$A = \frac{W}{p_m} \tag{2.5}$$

where

p_m flow pressure of soft surface
W applied load

For a normally distributed rough surface with the same profile curve in any section perpendicular to the y axis, as indicated in Fig. 2.24(b), A is given statistically by

$$A = \int_0^{L_y} L_x \frac{F(u)}{F(-m\sigma)}\,dy = L_x L_y \frac{F(u)}{F(-m\sigma)} = L_x L_y \frac{\Phi(t)}{\Phi(-m)} \tag{2.6}$$

where

$$F(u) = \int_u^{m\sigma} f(u)du$$

$$f(u) = \frac{1}{\sqrt{2\pi}\sigma} e^{-(1/2)(u/\sigma)^2}$$

$$\Phi(t) = \int_t^m \varphi(t)dt$$

$$\varphi(t) = \frac{1}{\sqrt{2\pi}} e^{-t^2/2}$$

σ standard deviation

m constant depending on surface roughness and type of surface finish ($m\sigma$ is distance between tip of highest asperity and median line of profile curve on considerably wide surface; m is determined experimentally from peak-to-valley height of profile curve on considerably wide surface)

$L_x L_y$ apparent contact area between two surfaces

Combining Eqs. (2.5) and (2.6) gives

$$L_x L_y \frac{\Phi(t)}{\Phi(-m)} = \frac{W}{p_m} \tag{2.7}$$

The distance (separation) between the ideal surface and the median line of the profile curve for the rough surface under applied load W can be given by

$$u = t\sigma \tag{2.8}$$

and the penetration depth of the ideal flat surface U is given by

$$U = (m\sigma - u) = (m - t)\sigma \tag{2.9}$$

When two rough surfaces having Gaussian height distribution are brought into contact, the contact also takes place over a small area, actually at the tips of the

asperities or surface irregularities, as indicated in Fig. 2.25(a). In this case, the probability density $g(w)$ of the contact is given by

$$g(w) = \frac{1}{\sqrt{2\pi}\sqrt{\sigma_1^2 + \sigma_2^2}} e^{-(1/2)\left(w/\sqrt{\sigma_1^2+\sigma_2^2}\right)^2} \tag{2.10}$$

where σ_1 and σ_2 are standard deviations of the two profile curves. This relation coincides with the probability density of contact between an ideal flat surface and a rough surface having a standard deviation of

$$\sigma = \sqrt{\sigma_1^2 + \sigma_2^2} \tag{2.11}$$

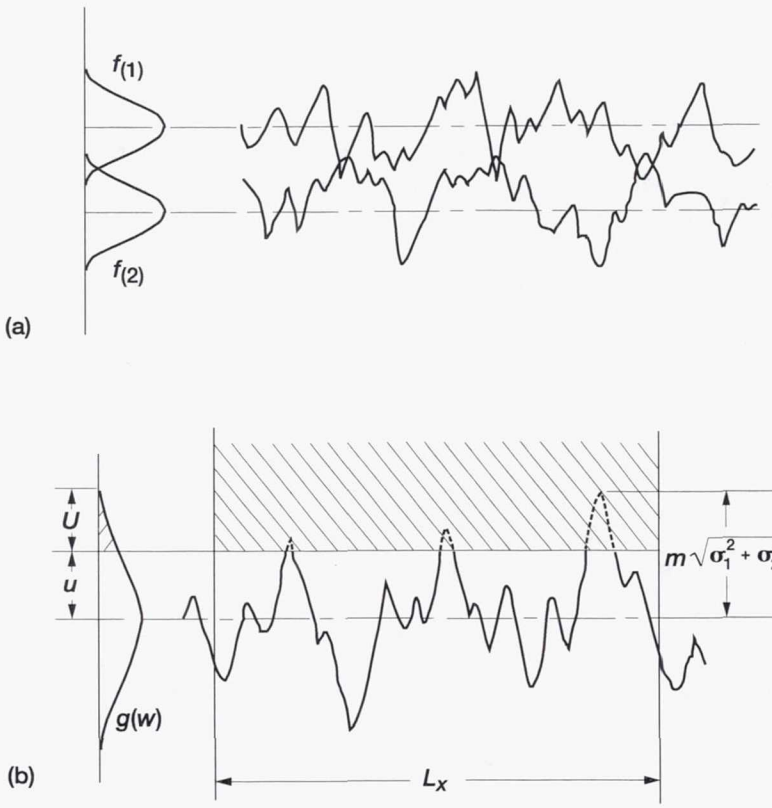

Figure 2.25.—Contact between two rough surfaces (a), and contact between ideal flat surface and rough surface having $\sqrt{\sigma_1^2 + \sigma_2^2}$ (b).

The separation w between two rough surfaces in contact is given by

$$w = t\sqrt{\sigma_1^2 + \sigma_2^2} \tag{2.12}$$

The penetration depth U is given by

$$U = (m - t)\sqrt{\sigma_1^2 + \sigma_2^2} \tag{2.13}$$

Thus, contact is limited to a relatively small area, and the rest of the surfaces are held apart. The real contact area and the interfacial gap can contribute significantly to all major aspects of tribology: adhesion, friction, lubrication, wear, corrosion, heat transfer and conductivity, electrical conductivity, seal or leakage, interference (shrinkage) fits, cylinder/cylinder liner tolerances, and more.

The interfacial gap formed is usually continuous, permitting gas and liquid access to the whole interface. Surface textures can be designed to provide a particular interfacial gap. The surfaces of mechanical seals, for example, can be smoothed by superfinishing, honing, or lapping to reduce gaseous or liquid leakage and further given noninterconnecting dimples to carry some lubricants to reduce wear. Conversely, the surfaces of heavy-duty sliding bearings can be made to have wide interfacial gaps to facilitate lubricant access and debris removal; with a second process they can also be given shallow-domed plateaus that can carry the load with little plastic deformation and hence little wear.

Another example, presented in Fig. 2.26, is a plain bearing having circumferential microgrooves that was developed for crankshaft and connecting-rod bearings in gasoline engines [2.36]. The microgrooved bearing shows superior conformability relative to normal plane bearings, resulting in a shorter time to establish the hydrodynamic lubrication regime, increased oil flow resulting in lower bearing temperature, and superior oil-retaining properties that prevent seizure for a considerable time (more than 50 min) after cutting off the supply of lubricating oil.

The textures of engineering surfaces used in tribological applications vary widely. Even single-crystal surfaces have a variety of surface defects depending on bulk defects and preparation, such as ledges in crystal faces and steps where dislocations emerge as large-scale shape deviations [2.30]. Brittle, inorganic crystals that are cleaved have flat, atomically smooth surfaces between surface cleavage steps. The cleavage steps in these materials, such as SiC, Al_2O_3, MgO, and Mn-Zn ferrite, occur along cleavage planes. Some metals, such as zinc, undergo brittle cleavage at cryogenic temperatures [2.37]. Other alterations in surface geometry can occur from other processes, such as growth steps that develop during solidification from the liquid state and during crystal growth.

Mechanical preparation techniques produce, in addition to the microstructural defects discussed in Section 2.2.2, another level of surface topographic defects (e.g., grooves (scratches), smears, cavities, grain pullout, cracks, porosity, and

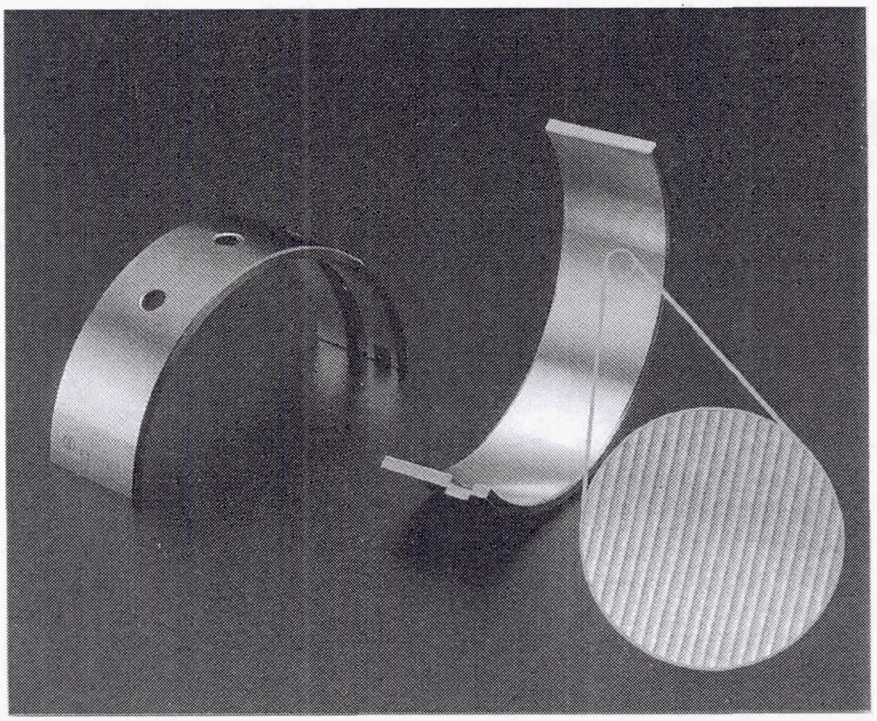

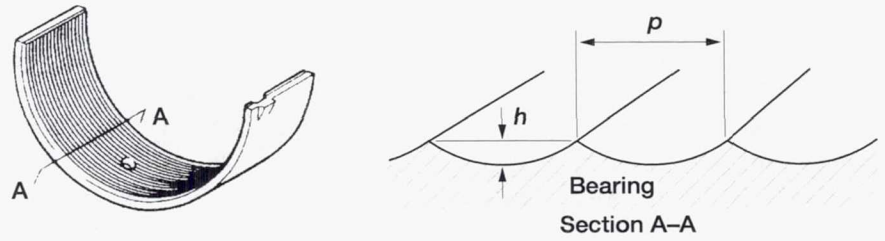

Figure 2.26.—Microgrooved bearing. Pitch, *p*, 0.20 to 0.25 mm; groove depth, *h*, 4.0 to 4.5 μm.

contamination (embedded foreign elements)). Grooves can be generated when a hard-surface particle rubs against a softer surface (two-body abrasion) or when small, hard particles are entrapped between two solid surfaces (three-body abrasion). Figure 2.11(a) shows a single-crystal Mn-Zn ferrite surface after two-body abrasion, and Fig. 2.12 shows the same surface after three-body abrasion [2.29]. The surfaces are covered with hills and valleys. The replication electron micrographs show a large number of plastically deformed grooves (Fig. 2.11(a)), brittle-fractured facets (Fig. 2.12(a)), and plastically deformed indentations and grooves (Fig. 2.12(b)). When the material is plastically pushed (i.e., moved across

the surface) instead of being cut, the resulting plastic deformation of a large area is called smearing. Cavities may be left after grains or particles are torn out of the solid surface. They are usually found in hard or brittle materials and in materials with inclusions. Hard or brittle materials can hardly be deformed plastically, so small parts of the surface material shatter and may fall out or be pulled out during machining or abrasion. Cracks occur in brittle materials and in materials with layers, such as coatings. Some materials have natural porosity (e.g., cast metals, spray coatings, and ceramics). Ceramics prepared by powder compaction and heat treatment are almost always porous. Deposits on a solid surface can serve as surface geometric irregularities. These deposits could include materials from a source other than the solid itself, such as wear and abrasive particles. Such contamination can occur on all types of material.

Another type of surface defect, the etch pit or line, can occur when the environment or a lubricant constituent reacts with the surfaces. Etch pits or lines can occur at high-energy sites (e.g, grain boundaries and subsurface defects, such as dislocation sites) after chemical, physical, or optical etching.

2.2.4 Contaminant and Oxide Layers

In addition to the presence of irregularities, commonly called asperities, as discussed in Section 2.2.3, the solid surface itself is covered with thin contaminant layers of atomic dimensions (~ 2 nm thick). These contaminant layers are unavoidably present on every surface of any solid matter that has been exposed to air. In other words, the simplest and most common occurrence recognized with real surfaces is that nearly all surfaces contain adsorbates, either physically adsorbed or chemically adsorbed material that has formed through interaction with the environment. Sometimes oxide layers of various depths are present beneath the surface contaminants. Knowledge of the contaminant and oxide layers is of great interest to materials researchers in tribology as modern technology tries to improve material properties, such as coefficient of friction and resistance against wear and corrosion in near-surface regions.

Figure 2.27 shows, for example, how the ambient atmosphere affects the dry surface of an elemental metal. A thin contaminant layer of adsorbates is present, as on the surface of any solid. It is made up of contaminants, such as adsorbed gases,

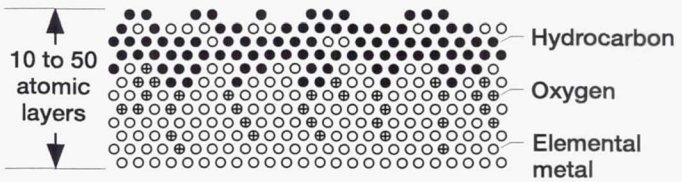

Figure 2.27.—Schematic model of metal exposed to air, showing contaminant layer.

water vapor, and hydrocarbons. Various hydrocarbons are detected if the component has been near operating machinery because lubricating or processing oils vaporize.

2.3 Surface Characterization Techniques

Although a wide range of physical surface analysis techniques is available, certain traits common to many of them can be classified from two viewpoints. Most techniques involve either electrons, photons (light), x rays, neutral species, or ions as a probe beam striking the material to be analyzed. The beam interacts with the material in some way. In some of these techniques the changes induced by the beam (energy, intensity, and angular distribution) are monitored after the interaction, and analytical information is derived from observing these changes. In other techniques the information used for analysis comes from electrons, photons, x rays, neutral species, or ions that are ejected from the specimen under the stimulation of the probe beam (Fig. 2.28). In many situations several connected processes may be going on more or less simultaneously, with a particular analytical

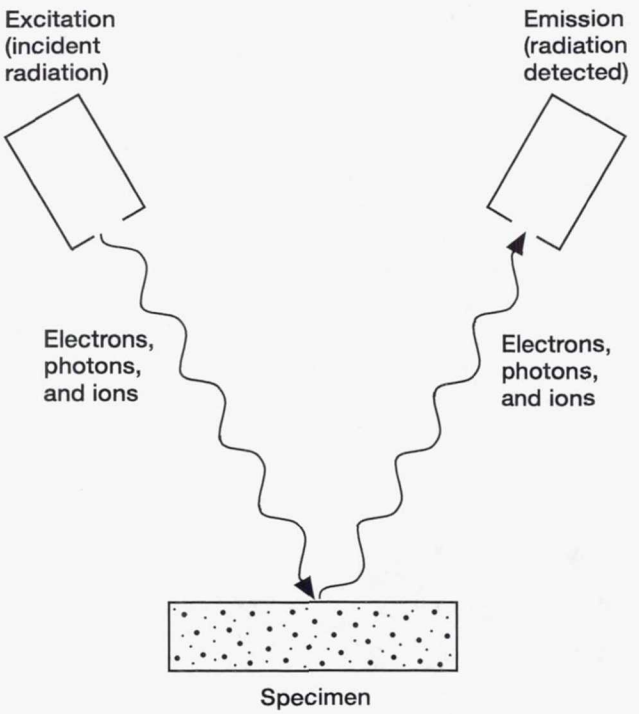

Figure 2.28.—Schematic diagram showing excitation and emission processes on solid surface.

TABLE 2.1.—POPULAR ANALYTICAL TECHNIQUES FOR SURFACE, THIN-FILM, INTERFACE, AND BULK ANALYSIS OF SOLID LUBRICANT ON SUBSTRATE

Technique	*Main information*	*Use* (popularity)
Light microscopy	Defects Image and morphology	Extensive
Scanning electron microscopy (SEM)	Defects Image and morphology	Extensive
Scanning tunneling microscopy (STM) and atomic force microscopy (AFM)	Structure Defects Image and morphology	Medium
Transmission electron microscopy (TEM)	Phase Structure Defects Image and morphology	Medium
Energy-dispersive x-ray spectroscopy (EDS)	Element composition Image	Medium
Electron energy-loss spectroscopy (EELS)	Element composition Chemical state Image	Not common
Cathodoluminescence (CL)	Element composition Defects	Not common
Electron probe x-ray microanalysis (EPMA)	Element composition Image	Medium
X-ray diffraction (XRD)	Phase Structure Defects	Extensive
Low-energy electron diffraction (LEED)	Structure Defects	Medium
Reflection high-energy electron diffraction (RHEED)	Structure Defects	Medium
X-ray photoelectron spectroscopy (XPS)	Element composition Chemical state Image	Extensive
Auger electron spectroscopy (AES)	Element composition Chemical state Image	Extensive
X-ray fluorescence (XRF)	Element composition	Extensive
Photoluminescence (PL), or fluorescence spectrometry	Chemical state Defects Image	Medium
Variable-angle spectroscopic ellipsometry (VASE)	Film thickness	Not common
Fourier transform infrared spectroscopy (FTIR)	Chemical state Defects	Extensive
Raman spectroscopy	Chemical state Defects	Medium
Solid-state nuclear magnetic resonance (NMR)	Chemical state Phase Structure	Not common
Rutherford backscattering spectrometry (RBS)	Element composition Structure Defects	Medium
Elastic recoil spectroscopy (ERS)	Hydrogen content	Not common

TABLE 2.1.—Concluded.

Technique	Main information	Use (popularity)
Ion-scattering spectroscopy (ISS)	Element composition	Not common
Secondary ion mass spectrometry (SIMS)	Element composition Chemical state Image	Extensive
Mass spectrometries: Sputtered neutral (SNMS) Laser ionization (LIMS) Spark source (SSMS) Glow discharge (GDMS) Inductively coupled plasma (ICPMS)	Element composition Chemical state	Extensive to medium
Profilometers: Stylus profiler Optical profiler	Surface roughness Image	Extensive
Adsorption	Surface areas Chemisorption	Medium

technique picking out only one aspect (e.g., the extent of incident light absorption or the kinetic energy distribution of ejected electrons).

Table 2.1 briefly summarizes the analytical techniques available to the solid lubricants user and tribologist today in studying the properties and behavior of solid surfaces. The table allows quick access to the type of information provided by the techniques and their popularity. The reader will find the basic principles and instrumentation details for a wide range of analytical techniques in the literature (e.g., [2.4–2.6, 2.9, 2.10]). However, the analytical instrumentation field is moving rapidly and within a year current spatial resolutions, sensitivities, imaging/mapping capabilities, accuracies, and instrument costs and size are likely to be out of date. Therefore, these references should be viewed with caution.

What types of information are provided by these analytical techniques? Elemental composition is perhaps the most basic information, followed by chemical state information, phase identification, the determination of structure (atomic sites, bond lengths, and angles), and defects.

The elemental and chemical state, phase, microstructure, and defects of a solid often vary as a function of depth into the material or spatially across the material, and many techniques specialize in addressing these variations down to extremely fine dimensions (on the order of angstroms in some cases). Requests are made for physical and chemical information as a function of depth to depths of 1 mm or so (materials have about 3 million atomic layers per millimeter of depth), as shown in Fig. 2.29. It is this region that affects a broad spectrum of properties: adhesion, bonding, friction, wear, lubrication, corrosion, contamination, chemical composition, and chemical activity. Knowledge of these variations is of great importance to the selection and use of solid lubricants and other tribological materials.

For surfaces, interfaces, and thin films there is often little material to analyze; hence, the presence of many microanalytical methods in Table 2.1. Within micro-

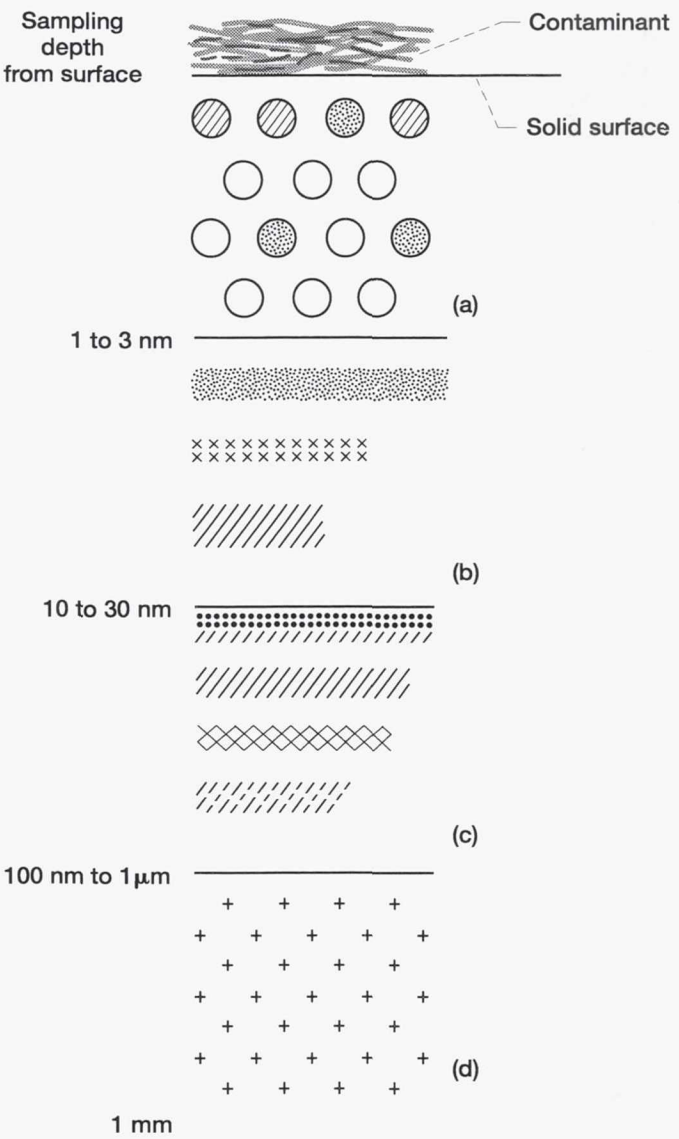

Figure 2.29.—Schematic diagram showing regimes of (a) surface analysis, (b) thin-film analysis, (c) interface analysis, and (d) bulk substrate analysis.

analysis it is often necessary to identify trace components down to extremely low concentrations (parts per trillion in some cases), and a number of techniques specialize in this aspect. In other cases a high degree of accuracy in measuring the presence of major components might be the issue. Usually, the techniques that are good for trace identification do not accurately quantify major components. Most complete analyses require the use of multiple techniques, the selection of which depends on the nature of the specimen and the desired information.

Figure 2.30 demonstrates the importance of the sampling (information) depth by comparing the analysis of two different specimens. The first has an atomic layer of impurity atoms on the surface; the other has these atoms distributed homogeneously within the specimen. When a conventional x-ray microprobe with a sampling depth of about 1000 nm is used, the specimens produce signals of equal intensity and it is not possible to differentiate between them. One can sometimes get an indication of whether there is a bulk impurity or a surface segregation (or a thin film) by lowering the electron beam voltage or by measuring at grazing incidence. However, this is not possible with only a few atomic layers. On the other hand, because of their insufficient detection limits Auger electron spectroscopy (AES) or x-ray photoelectron spectroscopy (XPS) will produce two quite different

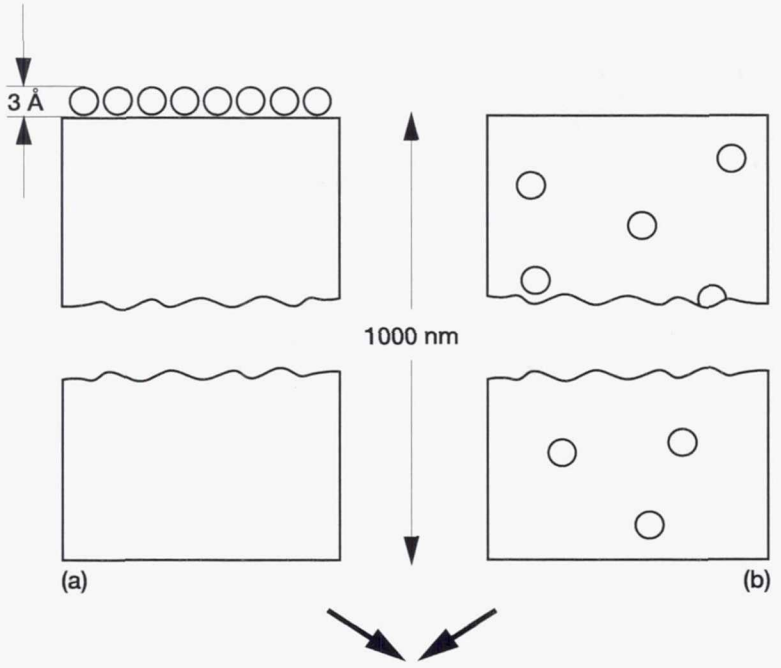

Figure 2.30.—Schematic diagram showing importance of information depth.
(a) Specimen 1: monolayer of foreign (impurity) atoms on surface.
(b) Specimen 2: same atoms with homogeneous distribution. (From [2.44].)

spectra: in the first specimen, a strong signal from the impurity layer caused by the low sampling depth; in the second specimen, only the spectrum of the pure bulk material with no indication of the impurities.

Figure 2.31 illustrates the information depth capabilities of surface-sensitive characterization tools (ion scattering spectroscopy (ISS), secondary ion

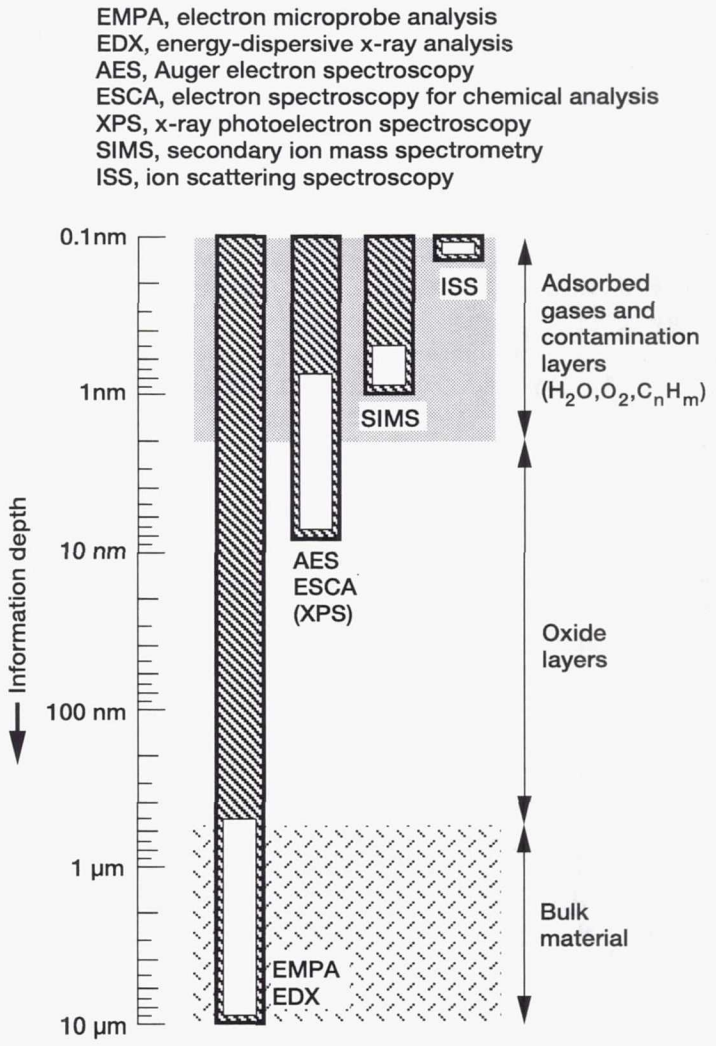

Figure 2.31.—Information depth capabilities of various surface analysis techniques. (The unshaded areas within the bars represent the variation of the information depths, which depend on instrumental parameters and on the material itself.) (From [2.44].)

mass spectrometry (SIMS), AES, and XPS, which is also called electron spectroscopy for chemical analysis (ESCA)) and of bulk characterization tools (electron microprobe analysis (EMPA) and energy-dispersive x-ray analysis (EDX)). Thus, knowing both the structure of real surfaces and the capabilities of the various characterization techniques is of great importance.

It was during the 1960's that the amazing growth and diversification of surface analytical techniques began and evolved with the development of two types of ultra-high-vacuum electron spectroscopy—Auger electron spectroscopy (AES) closely followed by x-ray photoelectron spectroscopy (XPS). The combination of the all-encompassing definition of tribology with these surface analytical techniques, including a variety of electronic, photonic, and ionic spectroscopies and microscopies, reflects the trend of tribology and solid-film lubricants today. In the following subsections characterization equipment commonly used in the fields of tribology and tribological coatings (including solid-film lubricants) and examples of their use are described. Also, it is shown where surface science can play a role in advancing our knowledge of adhesion, friction, lubrication, and wear as well as the basics of tribological phenomena.

A number of techniques are now available for measuring the composition of any solid surface. The most widely used techniques for surface analysis are AES, XPS (or ESCA), and SIMS. These techniques are well suited for examining extremely thin layers, including the contaminant layers and the oxide layers.

2.3.1 AES and XPS

The surface analytical techniques most commonly used in tribology are AES and XPS (or ESCA). Each can determine the composition of the outermost atomic layers of a clean surface or of surfaces covered with adsorbed gas films, oxide films, lubricants, reaction film products, and frictionally transferred films and can describe the surface [2.4–2.11].

AES and XPS are generally called "surface analysis" techniques, but this term can be misleading [2.5]. Although these techniques derive their usefulness from their intrinsic surface sensitivity, they can also be used to determine the composition of deeper layers. Such a determination is normally achieved through controlled surface erosion by ion bombardment. AES or XPS analyzes the residual surface left after a certain sputtering time with rare gas ions. In this way, composition depth profiles can be obtained that provide a powerful means for analyzing thin films, surface coatings, reaction film products, transferred films, and their interfaces. Clearly, this capability also makes AES and XPS ideal for studying wear-resistant coatings and solid-film lubricants. There are, however, a number of practical differences between the two techniques (e.g., detection speed, background, and spatial resolution, as shown in Table 2.2) that are generally more advantageous in AES profiling. Table 2.2 lists the methods and capabilities of AES and XPS, the two principal solid surface analysis techniques. Again,

TABLE 2.2.—CHARACTERISTICS OF AES AND XPS (OR ESCA) FOR PRACTICAL SURFACE ANALYSIS OF SOLID LUBRICANTS

Method and capabilities	Auger electron spectroscopy (AES)	X-ray photoelectron spectroscopy (XPS, or ESCA)
Excitation by–	Electrons	X rays
Detection of–	Electrons	Electrons
Destructive?	No, except to electron-beam-sensitive materials and during depth profiling	No, some beam damage to x-ray-sensitive materials
Element analysis?	Yes, semiquantitative without standards and quantitative with standards	Yes, semiquantitative without standards and quantitative with standards; not a trace element method
Range of elements	All except hydrogen and helium; no isotopes	All except hydrogen and helium; no isotopes
Sensitivity differences for range of elements	Factor of 10	Factor of 10
Detection limit	1000 ppm or 10^{-10} g/cm^3	1000 ppm or 10^{-10} g/cm^3
Chemical state information?	Yes, in many materials	Yes
Depth probed	0.5 to 10 nm	0.5 to 5 nm
Depth profiling?	Yes, in combination with ion beam sputtering	Yes, over the top 5 nm; greater depths require sputter profiling
Lateral resolution	30 nm for Auger analysis, even less for imaging	5 mm to 75 μm; down to 5 μm in special instruments
Imaging/mapping?	Yes, called scanning Auger microscopy (SAM)	Yes, called imaging XPS (or ESCA scope)
Sample requirements	Vacuum-compatible materials	Vacuum-compatible materials

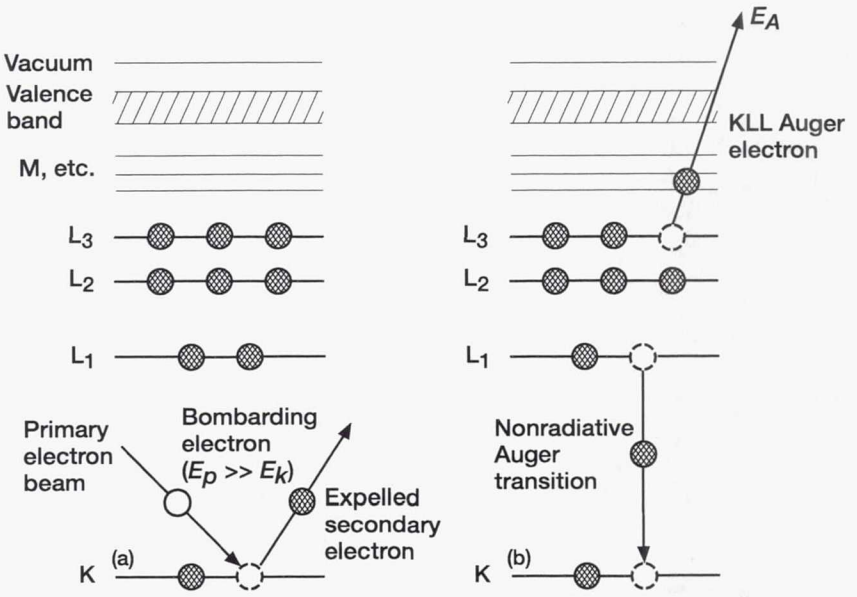

Figure 2.32.—Schematic diagram of Auger emission in a solid. (a) Excitation by electrons. (b) Emission of Auger electrons.

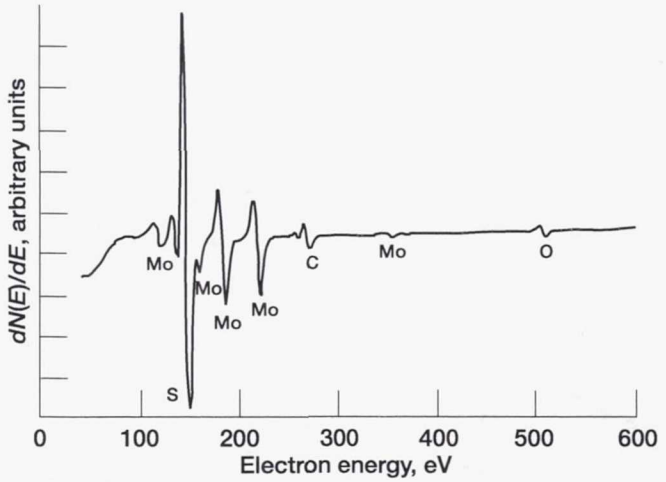

Figure 2.33.—AES spectrum from surface of slightly contaminated MoS_2 film deposited on AISI 440C stainless steel by magnetron radiofrequency sputtering.

because the instrumentation field is moving rapidly, this table should be viewed only as a reference and with caution.

AES.—AES uses a focused electron beam to create secondary electrons near a solid surface, as schematically shown in Fig. 2.32. Some of these electrons (the Auger electrons) have energies characteristic of the elements. Figure 2.33, for example, presents an AES spectrum of the surface of a molybdenum disulfide (MoS_2) film. The MoS_2 films were deposited by magnetron radiofrequency sputtering to a nominal thickness of 110 nm on sputter-cleaned AISI 440C stainless steel disk substrates. The MoS_2 films were exposed to air for a short time (less than 15 min) prior to AES analysis. A carbon contamination peak is evident as well as an oxygen peak. The presence of these peaks indicates that the MoS_2 surface is covered with oxides as well as a simple adsorbed film of contaminants, including oxygen and carbon. Adsorption of common contaminants, such as hydrocarbon vapor and water vapor, and oxidation easily take place on MoS_2 surfaces exposed to air. The contaminants and oxide films exist in layers of atomic dimensions. Note that the surface of the MoS_2 film shows a highly dense, smooth, featureless appearance by scanning electron microscopy.

As stated above, AES can characterize the specimen in depth and provide elemental depth profiles when used in combination with sputtering (e.g., argon-ion sputter etching) to gradually remove the surface. Figure 2.34 presents an example of an AES depth profile, with contaminant concentration shown as a function of sputtering distance from the MoS_2 film surface. The concentrations of sulfur (S) and molybdenum (Mo) at first rapidly increase with an increase in sputtering distance, whereas the concentrations of carbon (C) and oxygen (O)

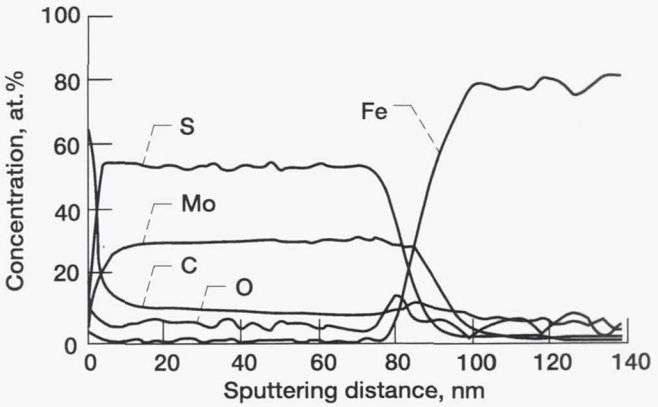

Figure 2.34.—AES depth profile of MoS_2 film on AISI 440C stainless steel.

initially decrease. They all remain constant thereafter. The MoS_2 film has a sulfur-to-molybdenum ratio of approximately 1.7. The relative concentrations of various constituents are determined by using manufacturers' sensitivity factors. Although the contaminants are removed from the film surface by sputtering, the MoS_2 film contains small amounts of carbon and oxygen impurities in the bulk.

In addition to energies characteristic of the elements, as shown in Fig. 2.32, some of the Auger electrons detected have energies characteristic, in many cases, of the chemical bonding of the atoms from which they are released. Because of their characteristic energies and the shallow depths from which they escape without energy loss, Auger electrons can characterize the elemental composition and, at times, the chemistry of surfaces. The Auger peaks of many elements show significant changes in position or shape in different chemical conditions and environments. For example, AES can distinguish between amorphous carbon, carbide, and graphite. Figures 2.35 and 2.36 compare the survey AES spectra and high-resolution AES spectra for carbon in various forms present on single-crystal SiC exposed to various environments. These AES spectra were obtained from three different surfaces: (1) a surface polished at room temperature, (2) a surface heated to 800 °C in ultrahigh vacuum, and (3) a surface heated to 1500 °C in ultrahigh vacuum. AES peaks of amorphous carbon, carbide, and graphite were detected from single-crystal SiC {0001} surfaces. When the polished single-crystal SiC is placed in a vacuum, one of the principal contaminants on the surface is adsorbed carbon. The high-resolution AES spectrum for carbon on the as-received surface appears only as the single main carbon peak, labeled A_0 in Fig. 2.36(a), where A is used to denote an AES peak. The carbon peak is similar to that obtained for amorphous carbon but not to that obtained for carbide. The high-resolution AES peaks for carbon on the SiC surface heated to 800 °C indicate a carbide peak, similar to that obtained for an SiC surface cleaned by argon-ion sputtering at room temperature. The carbide AES peaks are characterized by the

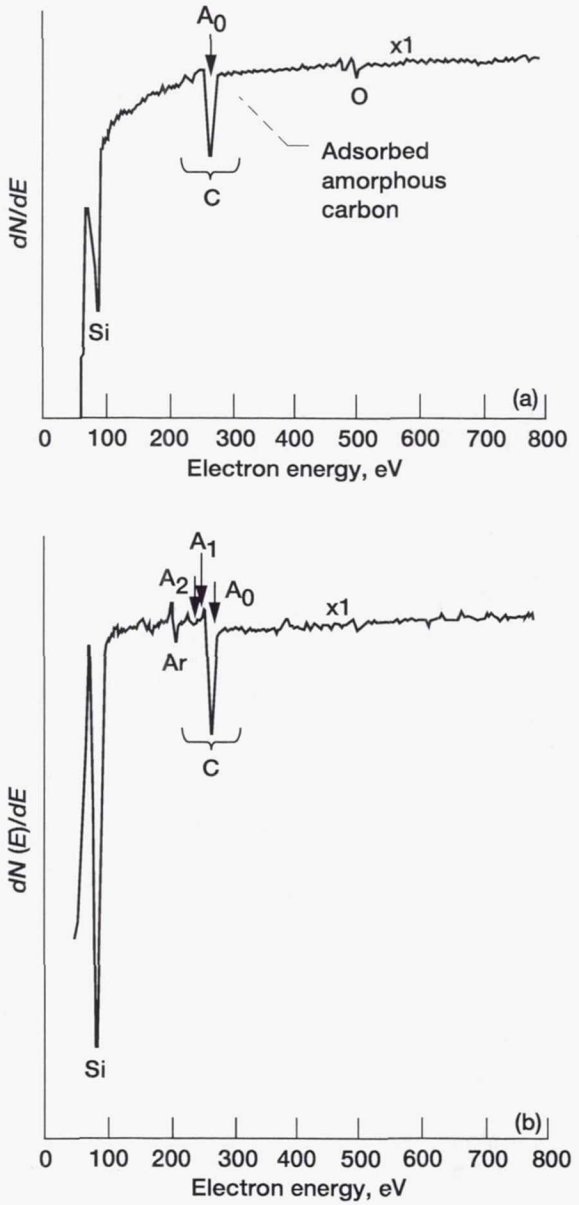

Figure 2.35.—Survey AES spectra of SiC {0001} surfaces treated in different conditions. (a) Polished surface at room temperature. (b) Surface heated to 800 °C in ultrahigh vacuum. (c) Surface heated to 1500 °C in ultrahigh vacuum.

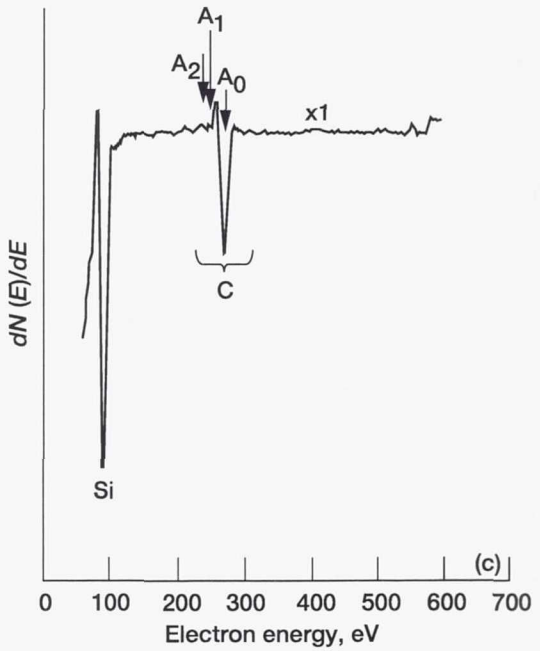

Figure 2.35.—Concluded. (c) Surface heated to 1500 °C in ultrahigh vacuum.

three peaks labeled A_0, A_1, and A_2 in Fig. 2.36(b). The high-resolution spectrum of the SiC surface heated above 1500 °C clearly reveals a graphite peak at 271 eV. The graphite form of carbon is characterized by a step labeled A in Fig. 2.36(c).

Furthermore, Fig. 2.37 presents a survey AES spectrum and a high-resolution AES spectrum for carbon obtained from a single-crystal {111} diamond surface after argon-ion sputter etching. The high-resolution spectrum has four peaks, as is characteristic of diamond. The peaks have been labeled A_0 to A_3. The energies of the peaks in this case are 267 to 269 eV for A_0, 252 to 254 eV for A_1, 240 eV for A_2, and 230 to 232 eV for A_3. The high-resolution AES spectrum is consistent with that obtained by other workers for a clean diamond surface [2.38].

Thus, AES has the attributes of high lateral resolution, relatively high sensitivity, and standardless semi-quantitative elemental analysis. It also provides chemical bonding information in some cases. Further, the high spatial resolution of the electron beam and the sputter etching process allow microanalysis of three-dimensional regions of solid specimens.

XPS.—In XPS monoenergetic soft x rays bombard a specimen material, causing electrons to be ejected, as shown in Fig. 2.38. The elements present in the specimen can be identified directly from the kinetic energies of these ejected photoelectrons. Electron binding energies are sensitive to the chemical state of the atom. Although the XPS is designed to deal with solids, specimens can be gaseous,

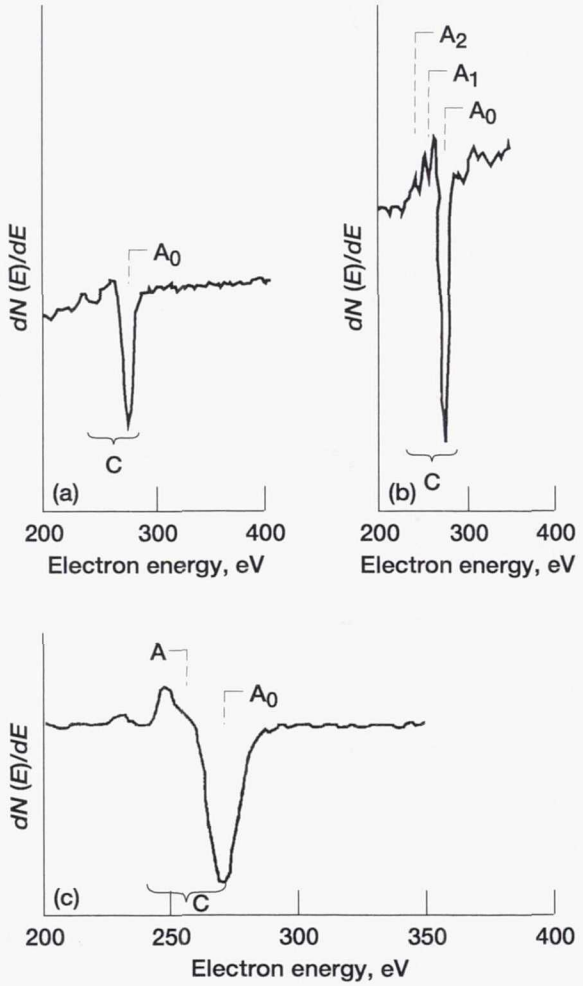

Figure 2.36.—High-resolution AES spectra of SiC {0001} surfaces treated in different conditions. (a) Amorphous carbon at room temperature. (b) Carbide at 800 °C. (c) Graphitic carbon at 1500 °C.

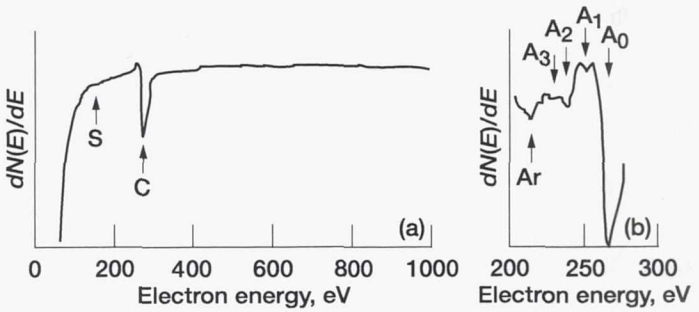

Figure 2.37.—AES spectrum for diamond. (a) Survey spectrum. (b) High-resolution spectrum.

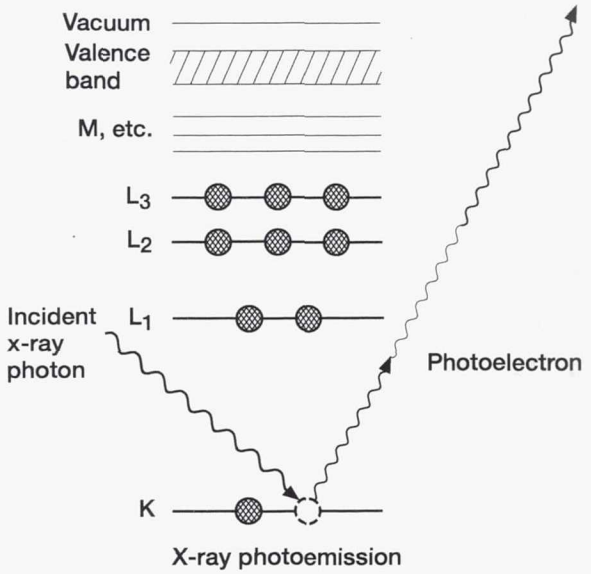

Figure 2.38.—Schematic energy level diagram illustrating photoexcitation of K-shell electron by low-energy x-ray photon.

liquid, or solid. XPS is applicable to metals, ceramics, semiconductors, organic, biological, and polymeric materials. Although x-ray beam damage can sometimes be significant, especially in organic materials, XPS is the least destructive of all the electron or ion spectroscopy techniques. The depth of solid material sampled varies from the top 2 atomic layers to 15 to 20 layers. This surface sensitivity, combined with quantitative and chemical analysis capabilities, has made XPS the most broadly applicable general surface analysis technique used today, especially in the field of tribology. Like AES, XPS can also characterize the specimen in depth

and provide elemental depth profiles when used in combination with sputtering (e.g., argon-ion sputter etching) to gradually remove the surface. Specific examples are given in the following paragraphs.

Figure 2.39 presents XPS survey spectra of the untreated and laser-annealed tungsten disulfide (WS_2) coatings taken with magnesium K_α radiation. The major elements present in both coatings were tungsten, sulfur, oxygen, and carbon. A small amount of nitrogen was present on the surface of the untreated specimen. XPS depth profiles showing the concentrations of the major elements as a function of depth from the surface were obtained from both coatings. The nitrogen on the untreated coating disappeared immediately upon sputtering and so is not included in the profiles. The depth profiles were made by recording high-resolution spectra of the W_{4f}, S_{2p}, O_{1s}, and C_{1s} regions, sputtering for 50 s, and repeating the procedure until the total sputter time reached 300 s. Under the conditions used, the sputter etch rate was 0.021 nm/s as calibrated on a tantalum pentoxide (Ta_2O_5) standard. The depth profiles were quantified by using sensitivity factors supplied by the instrument manufacturer. No standards were run.

The major difference in the XPS analyses of the two coatings is evident from the depth profiles shown in Fig. 2.40. In the untreated coating there was almost no carbon or oxygen below a depth of 3 nm. In the laser-annealed coating, on the other hand, carbon and especially oxygen persisted throughout the profile. The sulfur concentration in the laser-annealed coating was correspondingly less than that in the untreated coating, although the tungsten concentrations were about the same.

The high-resolution O_{1s} spectra taken after 300 s of sputtering confirmed the much greater oxygen concentration in the laser-annealed coating than in the untreated coating (Fig. 2.41). High-resolution S_{2p} spectra both from the surface (Fig. 2.42(a)) and from 6 nm deep (Fig. 2.42(b)) showed that sulfur was present as the sulfide at all levels in both coatings. In particular, any sulfate would give a peak at a much higher binding energy, as indicated on these spectra. The high-resolution W_{4f} spectra were composed of a poorly resolved 7/2 and 5/2 doublet in the 31-eV to 35-eV range and a $5p_{3/2}$ line around 37 eV (Fig. 2.43). The published positions of the 7/2 line for several possible tungsten compounds are indicated in Fig. 2.43(a). Each of these would have a corresponding 5/2 and $5p_{3/2}$ component.

In summary of XPS analysis the surface oxides, represented by the initial high oxygen concentrations in the depth profiles, were 1 to 2 nm deep. To a depth of 6 nm the untreated coating was relatively uncontaminated WS_2, but the laser-annealed coating contained high levels of oxygen and somewhat less carbon, which replaced sulfur in the coating. In all cases sulfur was present as the sulfide.

As presented above, on a finer scale the chemical state of the elements present can be identified from small variations in the kinetic energies. Another example is shown in Fig. 2.44. High-resolution photoelectron lines for C_{1s} of the SiC {0001} surface are split asymmetrically into doublet peaks. Three spectral features, which depend on the chemical nature of the specimen, can be observed: (1) two kinds of doublet peaks, (2) change of the peak vertical height, and (3) shift of the peaks.

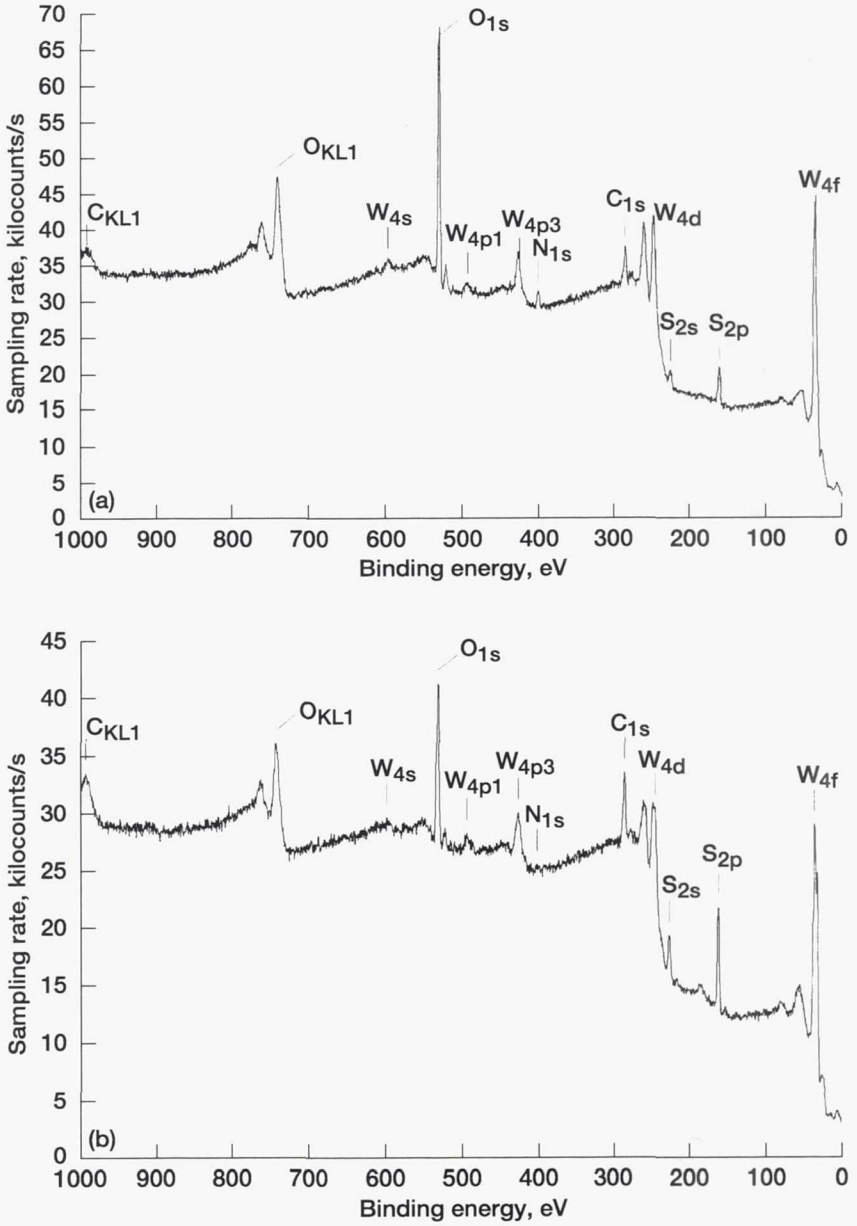

Figure 2.39.—Survey XPS spectra of pulse-laser-deposited WS_2 coatings. (a) Untreated. (b) Laser annealed.

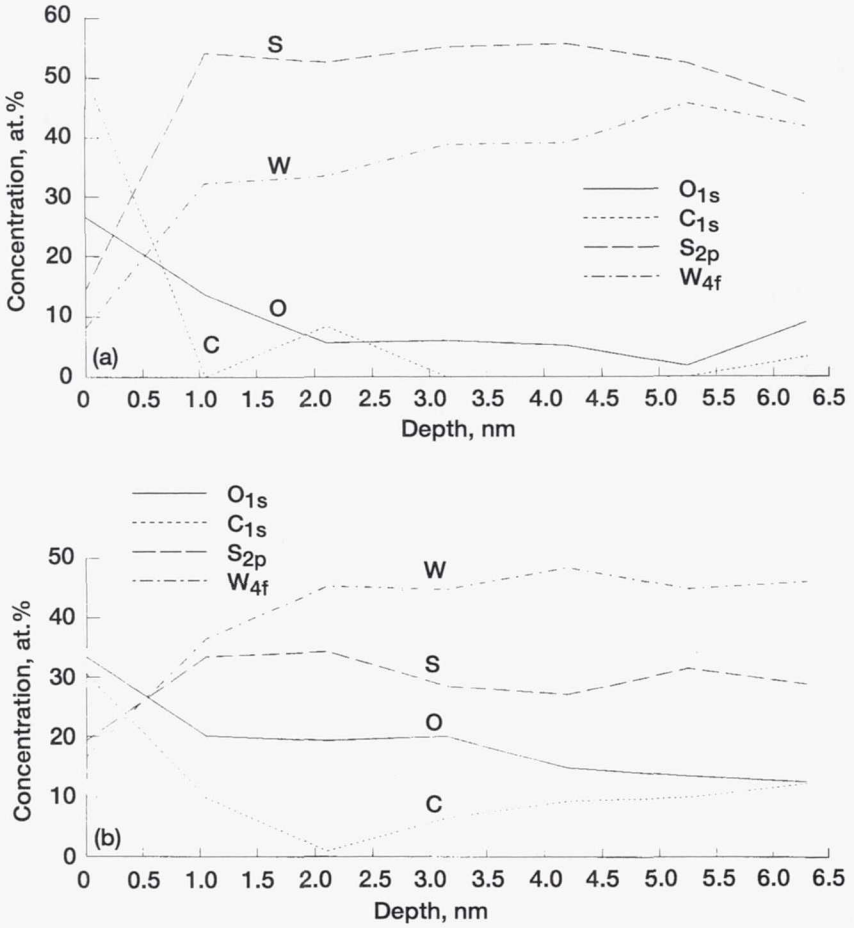

Figure 2.40.— XPS depth profiles of pulsed-laser-deposited WS_2 coatings. (a) Untreated. (b) Laser annealed.

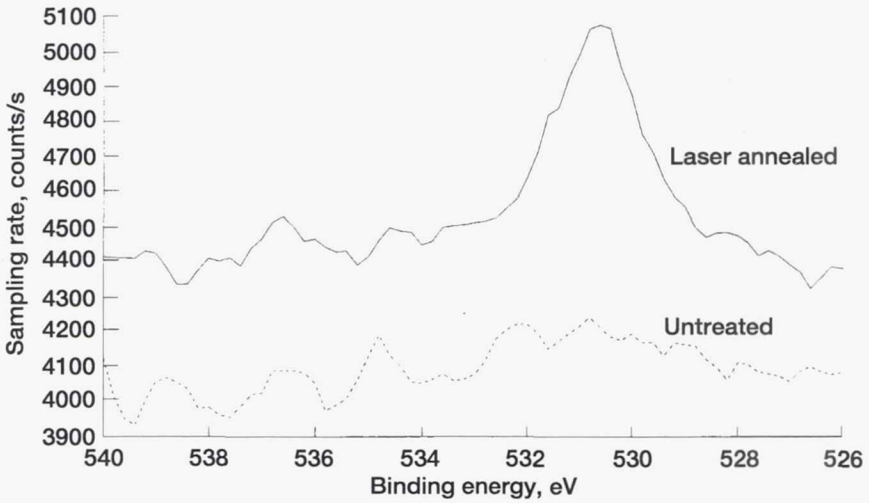

Figure 2.41.—O_{1s} spectra of pulsed-laser-deposited WS_2 coating after 300 s of sputtering.

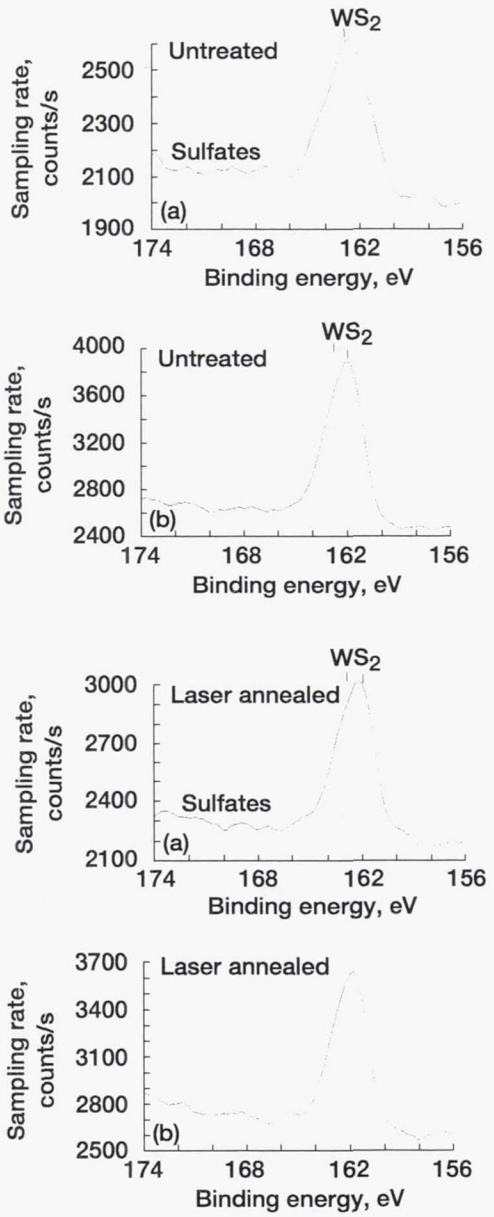

Figure 2.42.—High-resolution S_{2p} spectra of untreated and laser-annealed, pulsed-laser-deposited WS_2 coatings. (a) Surface. (b) After 300 s of sputtering from 6 nm deep.

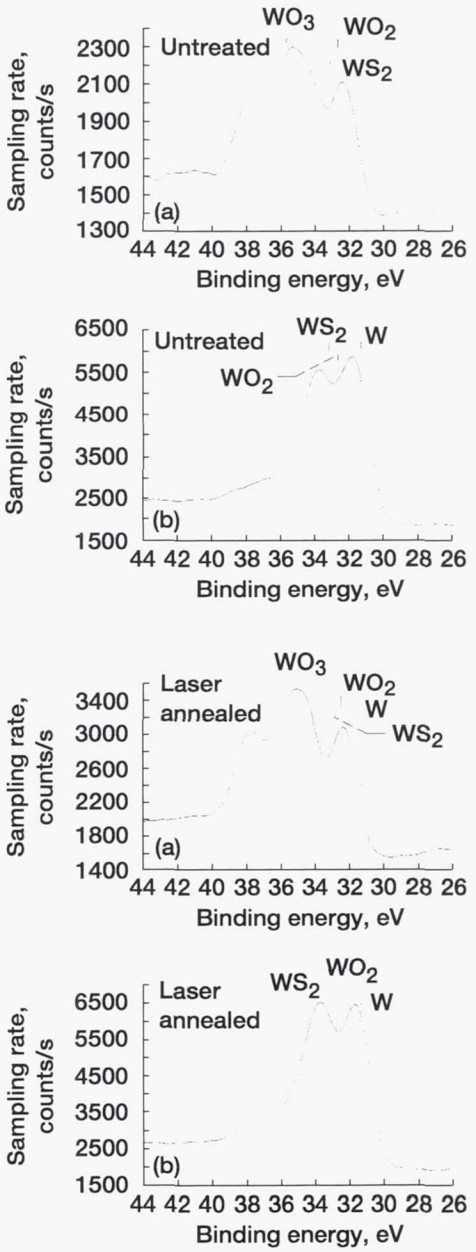

Figure 2.43.— High-resolution W_{4f} spectra of pulsed-laser-deposited WS_2 coatings. (a) Surface. (b) After 300 s of sputtering from 6 nm deep.

The XPS spectra of the as-received surface indicate distinguishable kinds of carbon (i.e., a carbon contamination peak and a carbide peak associated with the SiC). At room temperature the carbon contamination peak is higher than the carbide peak (Fig. 2.44(a)). At 800 °C the carbide peak is much higher than the graphite peak (Fig. 2.44(b)). At 1500 °C the spectra indicate a large graphite peak and a small carbide peak (Fig. 2.44(c)), as is typical of the surface heated above 800 °C.

The XPS carbon peaks (Fig. 2.44) are similar to the AES carbon peaks (Fig. 2.36). AES and XPS provide both elemental and chemical information for

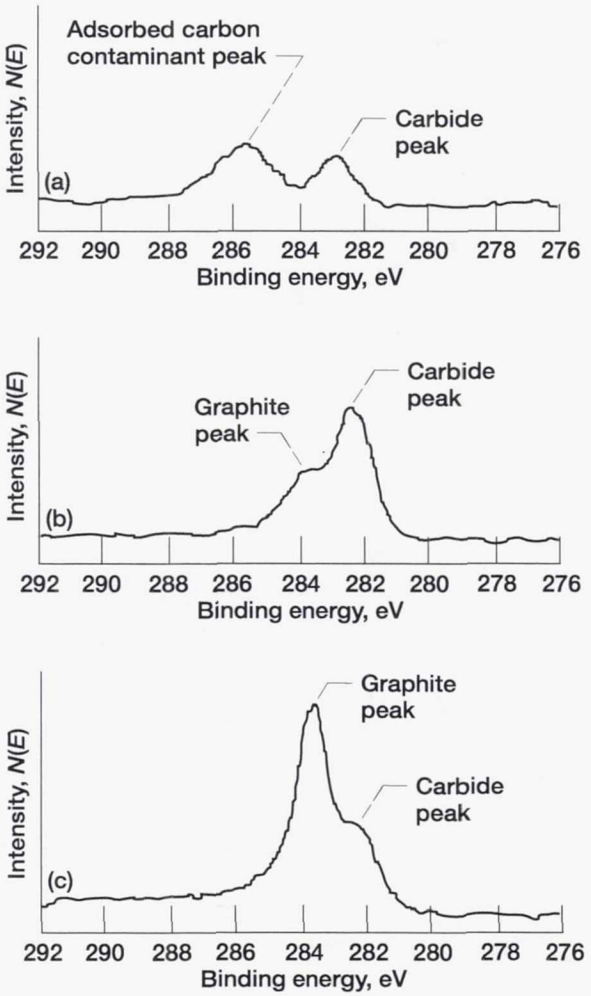

Figure 2.44.—Carbon XPS peaks on SiC.
(a) Room temperature. (b) 800 °C. (c) 1500 °C.

carbon in various forms present on single-crystal SiC. In general, AES provides elemental information only. The AES peaks of many elements, however, show significant changes in position or shape in different chemical environments. It is possible to distinguish among amorphous carbon, carbide, and graphite in AES, as demonstrated in Fig. 2.36. On the other hand, the main advantage of XPS is its ability to provide chemical information from the shifts in binding energy. The particular strengths of XPS are quantitative elemental analysis of surfaces (without standards) and chemical state analysis.

For a solid, AES and XPS probe 2 to 10 and 2 to 20 atomic layers deep, respectively, depending on the material, the energy of the photoelectron concerned, and the angle (with respect to the surface) of the measurement. Note that the AES analysis of SiC heated to 1500 °C (Fig. 2.36(c)) indicates that the carbon peak shown was only of graphite form. The XPS analysis (Fig. 2.44(c)), however, indicates that carbide as well as graphite was present on the SiC surface heated to 1500 °C. This difference can be accounted for by the fact that the analysis depth (sampling depth) with XPS is deeper.

The thickness of the outer graphite layer can be determined as follows: (1) by studying the attenuation by the graphite layer of photoelectrons originating in the bulk SiC material and (2) by studying the variation in intensity of photoelectrons emitted by the layer itself as a function of thickness. The photoelectron flux penetrating a layer thickness d is simply

$$I_d = I_0 \exp(-d/\lambda) \tag{2.14}$$

where I_d is the flux emerging at the surface (i.e., the XPS peak intensity from the layer of thickness d), I_0 is the flux emitted by the clean SiC, and λ is variously referred to as the inelastic mean free path, the mean escape depth, or the attenuation length of an electron having an electron energy within the material.

On the other hand, the intensity of a photoelectron signal from the layer is

$$I_d = I_0\{1 - \exp(-d/\lambda)\} \tag{2.15}$$

In either case, the mean escape depth λ relates to the layer material and to electrons of a given kinetic energy. The potential value varies with the angle of electron emission, or takeoff angle θ, in the XPS analysis. The generalized theoretical prediction for intensity changes with θ for the bulk SiC plus the graphite overlayer system is given by

$$I_d = I_0\{1 - \exp[-d(\lambda \sin\theta)]\} \tag{2.16}$$

Table 2.3 shows inelastic mean free paths of various elements and the estimated thickness of the graphite layer formed on the SiC surface. These values have been estimated by using Eqs. (2.14) to (2.16) and the values of λ for silicon, carbon, and

TABLE 2.3.—THICKNESS OF GRAPHITIC CARBON LAYER ON SiC SURFACE PREHEATED TO 1500 °C

Element and photoelectron, Mg K_α	Electron inelastic mean free path, λ, nm	Layer thickness, d, nm
Si_{2p}	[a]4.7	2.0
	[a,b] 3.9	1.7
C_{1s}	[b]4.4	1.8
Graphite C_{1s}	[a]2.1	1.5
	[a]3.1	2.3
	[a]3.4	2.4

[a]From [2.39]
[b]From [2.40]

graphite [2.39, 2.40]. Table 2.3 suggests that carbon collapse in two or three successive SiC surficial layers after silicon evaporation is the most probable mechanism for SiC surface graphitization. The outermost surficial graphite layer on the SiC heated to 1500 °C was 1.5 to 2.4 nm thick. These thicknesses suggest that carbon collapse in three successive SiC layers was the most probable mechanism for the initial graphitization stages of the SiC basal planes. Similar results were also obtained with sintered polycrystalline SiC.

2.3.2 SEM and EDS

The single most useful tool available today to tribologists and lubrication engineers interested in studying the morphology, defects, and wear behavior of tribological surfaces is undoubtedly the scanning electron microscope (SEM). Especially, the combination of the SEM and x-ray analysis utilizing either energy-dispersive x-ray spectroscopy (EDS) or wavelength-dispersive x-ray spectroscopy (WDS) provides a powerful tool for local microchemical analysis [2.10, 2.41]. The use of electron microprobe techniques in the SEM is now a well-established procedure. The two techniques, EDS and WDS, differ only in the use of an energy-dispersive, solid-state detector versus a wavelength-dispersive crystal spectrometer. Successful studies have been carried out to characterize the surfaces of bearings, seals, gears, magnetic recording components, and other manufactured sliding or rolling surfaces and to select tribological materials and solid lubricants for mechanisms with improved reliability and life.

The SEM is often the first analytical instrument used when a quick look at a material is required and the light microscope no longer provides adequate spatial resolution or depth of focus. The SEM provides the investigator with a highly magnified image of a material surface. Its resolution can approach a few nanometers and it can be operated at magnifications from about 10X to 300 000X. The SEM produces not only morphological and topographical information but information concerning the elemental composition near surface regions.

In the SEM an electron beam is focused into a fine probe and subsequently raster scanned over a small rectangular area. As the electron beam interacts with the specimen, it creates various signals, such as secondary electrons, internal currents, and photon emissions, all of which can be collected by appropriate detectors. The SEM–EDS produces three principal images: secondary electron images, backscattered electron images, and elemental x-ray maps (Fig. 2.45). Secondary and backscattered electrons are conventionally separated according to their energies. They are produced by different mechanisms. When a high-energy primary electron interacts with an atom, it undergoes either inelastic scattering with atomic electrons or elastic scattering with the atomic nucleus. In an inelastic collision with an electron some amount of energy is transferred to the other electron. If the energy transferred is extremely small, the emitted electron will probably not have enough energy to exit the surface. If the energy transferred exceeds the work function of the material, the emitted electron will exit the solid. When the energy of the emitted electron is less than about 50 eV, by convention it is referred to as a secondary electron (SE), or simply a secondary. Most of the emitted secondaries are produced within the first few nanometers of the surface. Secondaries produced much deeper in the material suffer additional inelastic collisions, which lower their energy and trap them in the interior of the solid.

Higher energy electrons are primary electrons that have been scattered without loss of kinetic energy (i.e., elastically) by the nucleus of an atom, although these collisions may occur after the primary electron has already lost some energy to inelastic scattering. Although backscattered electrons (BSE's) are, by definition, electrons that leave the specimen with only a small loss of energy relative to the primary electron beam energy, BSE's are generally considered to be the electrons that exit the specimen with an energy greater than 50 eV, including Auger electrons. The BSE imaging mode can be extremely useful for tribological applications, since the energy, spatial distribution, and number of BSE's depend

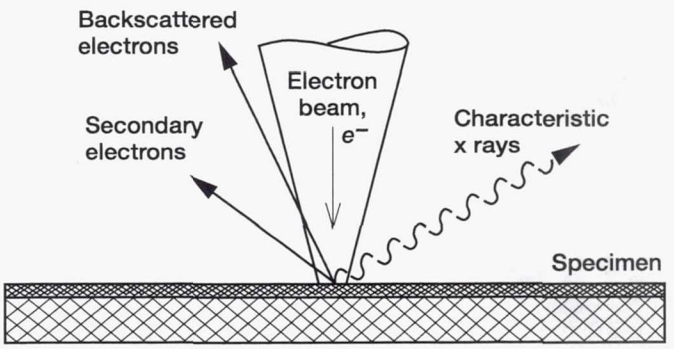

Figure 2.45.—Signals generated when focused electron beam interacts with specimen in scanning electron microscope.

on the effective atomic number of the specimen, its orientation with respect to the primary beam, and the surface condition. The backscatter coefficient, or relative number of electrons leaving the specimen, increases with increasing atomic number, as shown in Fig. 2.46 [2.41]. The higher the atomic number of a material, the more likely it is that backscattering will occur. Thus, as a beam passes from a low-Z (atomic number) to high-Z area, the signal due to backscattering and consequently the image brightness will increase. There is a built-in contrast caused by elemental differences. BSE images can therefore be used to distinguish different phases, transferred films, coatings, and foreign species of the specimen having different mean atomic numbers (atomic number contrast). For most specimens examined in SEM, except for those that are flat or polished, the specimen both varies in chemistry from area to area and exhibits a varying rough surface. As a result, both atomic number and topographic contrast are present in the BSE signal (as well as in the SE signal). In general, if the high-energy BSE's are collected from the specimen at a relatively high takeoff angle, atomic number information is emphasized. Conversely, if the high-energy electrons leaving the

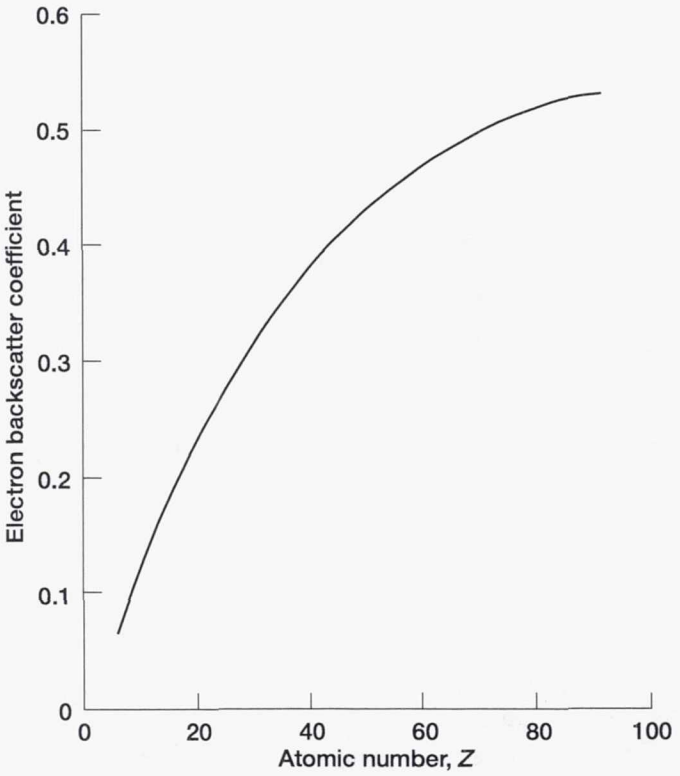

Figure 2.46.—Electron backscatter coefficient as function of atomic number.

specimen are collected at a relatively low takeoff angle, topographic information is emphasized. For nearly all BSE applications the investigator is interested in the atomic number contrast and not in the topographic contrast. Note that the backscatter coefficient is defined as the number of BSE's emitted by the specimen for each electron incident on the specimen. Because of the relatively deep penetration of the incident electron beam combined with the extensive range of the BSE's produced, spatial resolution in the BSE mode is generally limited to about 100 nm in bulk specimens under the usual specimen/detector configurations.

Both energy-dispersive and wavelength-dispersive x-ray detectors can be used for element detection in the SEM. When the atoms in a material are ionized by high-energy radiation, usually electrons, they emit characteristic x rays (Fig. 2.45). The detectors produce an output signal that is proportional to the number of x-ray photons in the area under electron bombardment. EDS is a technique of x-ray spectroscopy that is based on the collection and energy dispersion of characteristic x rays. Most EDS applications are in electron column instruments like the SEM, the electron probe microanalyzer (EPMA), and the transmission electron microscope (TEM). X rays entering a solid-state detector, usually made from lithium-drifted silicon, in an EDS spectrometer are converted into signals that can be processed by the electronics into an x-ray energy map or an x-ray energy histogram. A common application of the x-ray systems, such as EDS and WDS, involves x-ray mapping, in which the concentration distribution of an element of interest is displayed on a micrograph. The detectors can be adjusted to pass only the pulse range corresponding to a particular element. This output can then be used to produce an x-ray map or an elemental image. Higher concentrations of a particular element yield higher x-ray photon pulse rates, and the agglomeration of these pulses, which appear as dots in the image, generate light and dark areas relating to the element concentration distribution. In x-ray spectroscopy the x-ray spectrum consists of a series of peaks that represent the type and relative amount of each element in the specimen. The number of counts in each peak can be further converted into elemental weight concentration either by comparison with standards or by standardless calculations. Three modes of analysis are commonly used: spectrum acquisition; spatial distribution or dot mapping of the elements; and element line scans.

Figures 2.47 and 2.48 present examples of secondary electron images, backscattered electron images with both atomic number contrast and topographic contrast, and elemental x-ray maps. These examples were taken from the wear surfaces of a WS_2-film lubricant deposited on an AISI 440C stainless steel disk in sliding contact with a bare AISI 440C stainless steel ball in ultrahigh vacuum for approximately 500 000 disk revolutions. Figures 2.47(a) and 2.48(a) show secondary electron images taken with a primary energy of 20 keV on the disk wear track and the ball wear scar, respectively. The surfaces of the wear track and the wear scar are generally smooth. Likewise, most of the loose wear debris has accumulated on the outside of both the wear track and the wear scar. The darkest areas are

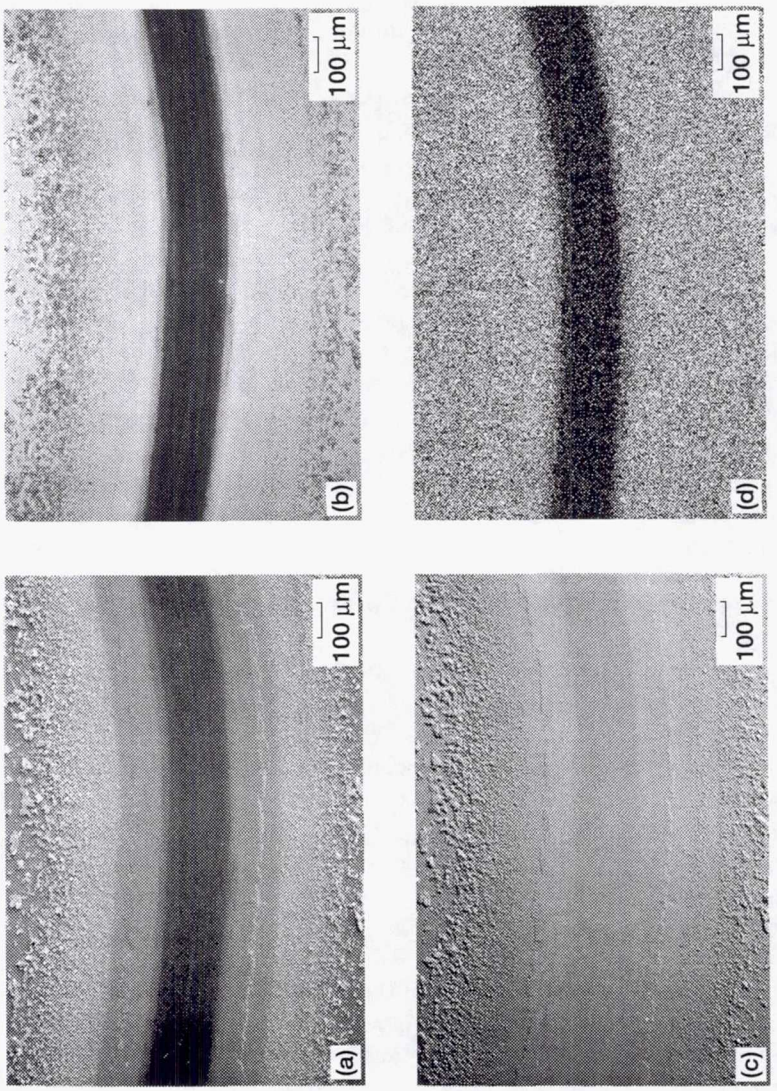

Figure 2.47.—Wear track on WS_2-film-lubricated AISI 440C stainless steel disk. (a) Secondary electron images. (b) Backscattered electron images with atomic number contrast. (c) Backscattered electron images with topographic contrast. (d) X-ray maps.

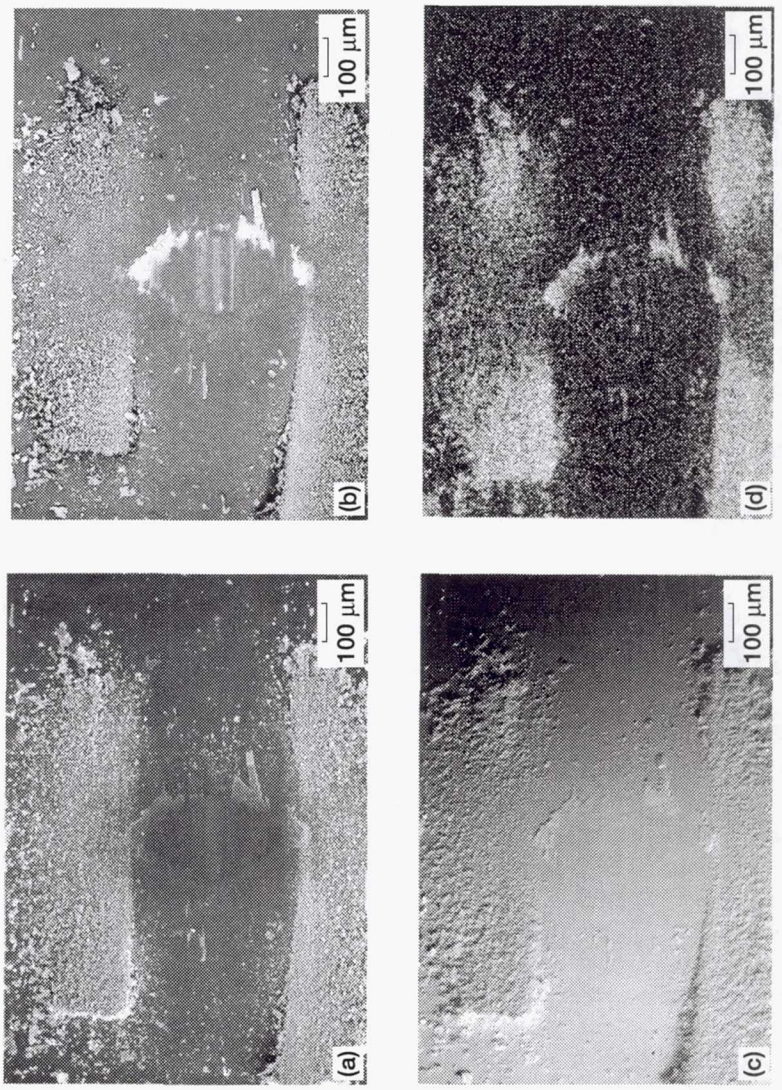

Figure 2.48.—Wear scar on AISI 440C steel ball. (a) Secondary electron images. (b) Backscattered electron images with atomic number contrast. (c) Backscattered electron images with topographic contrast. (d) X-ray maps.

essentially AISI 440C stainless steel. The light gray areas are essentially WS_2 wear debris. Darker gray areas, later identified as WS_2-film lubricant, are interveined. Secondary electron imaging generally yields better resolution than backscatter imaging (Figs. 2.47(b) and (c) and 2.48(b) and (c)) and x-ray maps (Figs. 2.47(d) and 2.48(d)). Clearly, chemistry plays an important role in developing image contrast or varying signal when imaging secondary electrons. In other words, a major contribution to the secondary electron image is generated by BSE's.

Figures 2.47(b) and (c) and 2.48(b) and (c) show atomic-number-contrast and topographic-contrast BSE images of the ball and disk, respectively. Atomic number contrast can be used to distinguish two materials, AISI 440C stainless steel and WS_2, because the actual BSE signal increases somewhat predictably with the concentration of the heavier element of the pair, as described above. In other words, higher Z (atomic number) areas should always be bright owing to the higher backscatter coefficient. In the present example (Figs. 2.47(b) and 2.48(b)) the light areas in the backscatter photomicrographs show where the most WS_2-film lubricant is present, and the dark areas show the AISI 440C stainless steel where no or less WS_2-film lubricant is present.

The topographic contrast information in Figs. 2.47(c) and 2.48(c) clearly indicates WS_2 wear debris on both wear track and wear scar, smeared WS_2 film on both sides of the wear track, and transferred WS_2 film on the wear scar. Even though for nearly all BSE applications the investigator is interested in the atomic number contrast and not in the topographic contrast, the topographic contrast of the BSE imaging mode can be extremely useful in solid lubricant investigations, especially wear analysis of solid lubricants. The tungsten (M_α, L_α, and L_β) and sulfur (K_α and K_β) x-ray maps in Fig. 2.47(d) and 2.48(d), respectively, are quite revealing. Areas of the WS_2 wear debris, WS_2 transferred films, and WS_2-film lubricant yield a high x-ray count. Major chemistry differences are quite obvious.

With EDS the output signal is displayed as a histogram of counts versus x-ray energy displays. The x-ray energy spectrum shown in Fig. 2.49(a) was produced by allowing the electron beam to dwell on one of the WS_2-wear-debris-rich areas deposited on the WS_2 film coating the disk specimen. The spectrum shows the presence of peaks corresponding to tungsten and sulfur and a small amount of iron (Fe) and chromium (Cr) from the AISI 440C stainless steel substrate material. Because this specimen was slightly contaminated with carbon and oxygen during deposition of the WS_2 film onto the substrate, the small carbon and oxygen peaks were expected. The spectrum shown in Fig. 2.49(b) was produced by allowing the electron beam to dwell on one of the WS_2-wear-debris-rich areas deposited on the counter material (the AISI 440C stainless steel ball specimen). The spectrum shows the presence of peaks corresponding to tungsten and sulfur and a large amount of iron and chromium from the AISI 440C stainless steel ball material. Small amounts of carbon and oxygen are also present in the spectrum.

Note that when examining a micrograph it is important to remember that the average human eye may perceive a spatial resolution on the order of 0.2 mm.

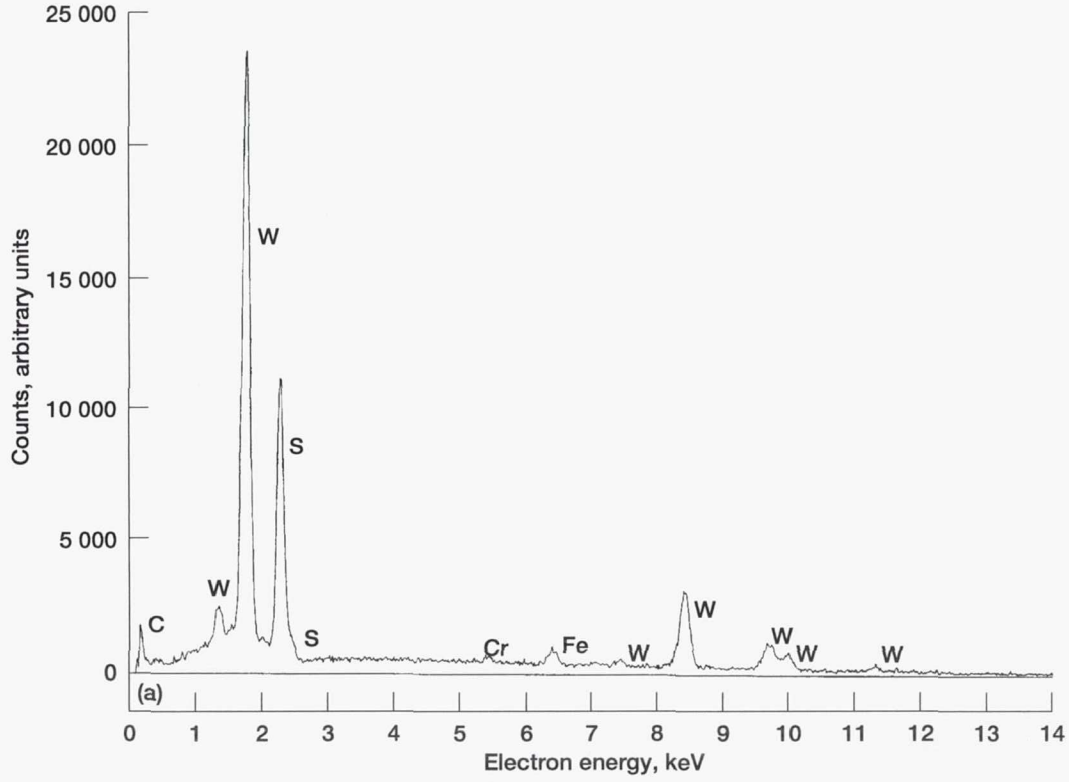

Figure 2.49.—X-ray energy spectra with EDS. (Sliding materials same as in Fig. 2.47.) (a) WS_2-film-coated AISI 440C stainless steel disk. (b) AISI 440C stainless steel ball.

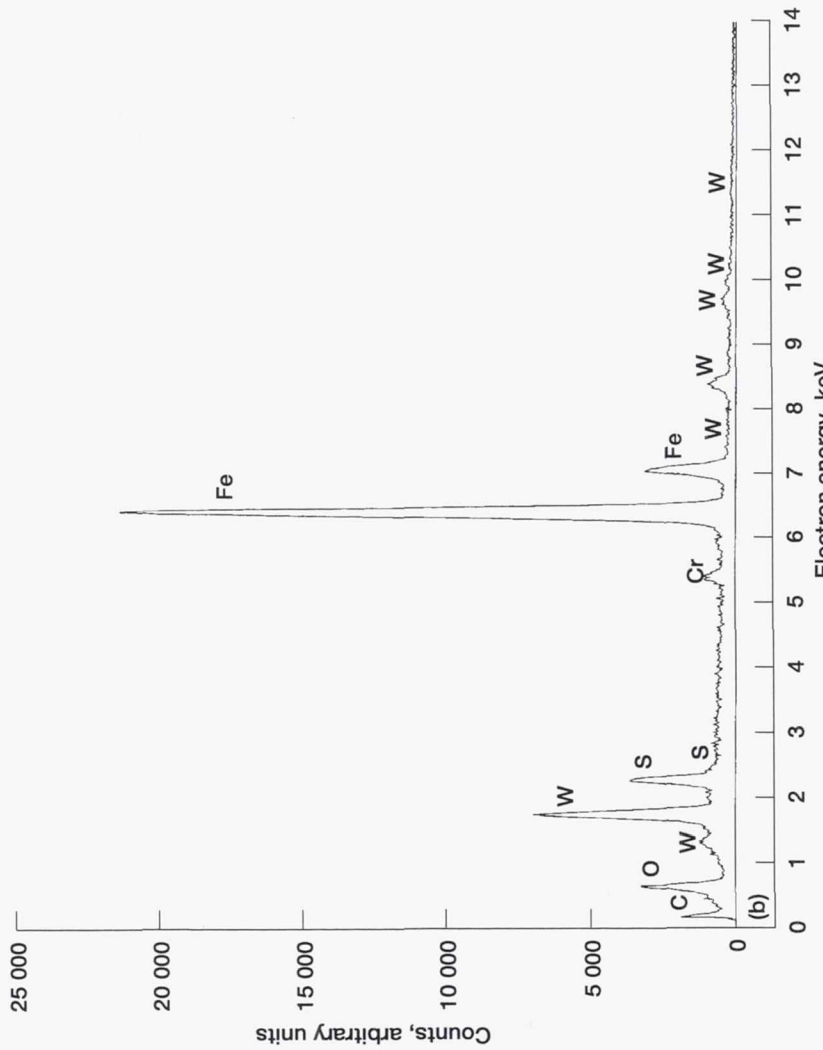

Figure 2.49.—Concluded. (b) AISI 440C stainless steel ball.

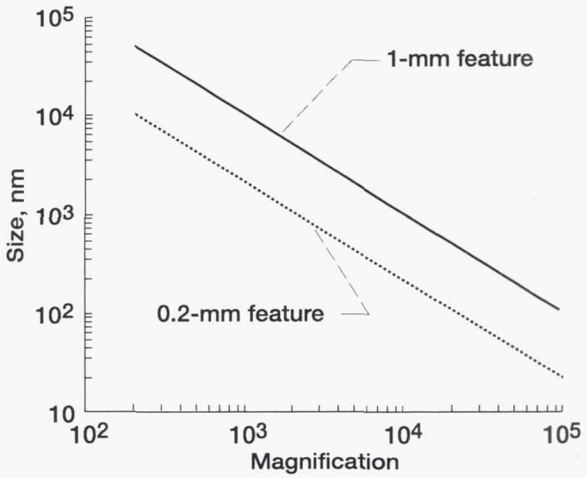

Figure 2.50.—True sizes of 1-mm image feature and 0.2-mm image feature (size of smallest feature resolvable by human eye) in photomicrograph as function of scanning electron microscope's magnification.

Figure 2.50 presents the size of a 1-mm feature in a micrograph as a function of magnification. The size of the smallest feature resolvable by the human eye (0.2 mm) is also given [2.41]. The magnification relates to the final magnification (including enlargement if done) of the micrograph. Figure 2.50 indicates that for a photomicrograph to appear perfectly sharp to the eye at 20 000X magnification, the instrument or electron optical resolution must be 10 nm or better.

2.4 Surrounding Environments

The environment may be a conventional, normal atmospheric condition, such as air in the terrestrial environment and vacuum in space, or some artificially imposed environment, such as inert gas, reactive gas, or liquid lubricant.

2.4.1 *Substances in Environments*

Substances in the surrounding environment have physical, chemical, and mechanical effects on the composition, structure, chemical state, and electronic state of the surfaces of tribological components and solid lubricating films in their formations, reactions, and combinations. Most substances in the surrounding environment fall under the categories of organic materials, inorganic materials, radiation, and/or vacuum ([2.42] and Table 2.4).

TABLE 2.4.—SUBSTANCES IN SURROUNDING ENVIRONMENT

Organic substances			Inorganic substances			Radiation	Vacuum
Solids	Liquids	Gases	Solids	Liquids	Gases		
Polymers Natural resins Living organisms Soils Foods	Lubricants Chemicals Fuels Oils Paints Foods	Hydrocarbons Carbon oxides	Metals Ceramics Composites Glasses Stone Lubricants (e.g., MoS_2 and graphite)	Water Acids Bases Drugs	Oxygen Nitrogen Argon Helium Sulfur Chlorine Atomic oxygen Ozone	Gamma rays X rays Ultraviolet Visible spectra Infrared Hertzian waves	Industrial vacuum processes Low vacuum ($>10^2$ to 10^5 Pa) Medium vacuum (10^{-1} to 10^2 Pa) High vacuum (10^{-5} to 10^{-1} Pa) Ultrahigh vacuum ($<10^{-5}$ Pa) Outer space (10^{-4} to 10^{-9} Pa)

TABLE 2.5.—WAVELENGTHS OF VARIOUS TYPES OF RADIATION

Type of radiation	Wavelength, μm
Gamma rays	0.005 to 0.140
X rays	0.01 to 10
Ultraviolet[a]	<400
Visible spectrum	400 to 700
Violet (representative, 410 μm)	400 to 424
Blue (representative, 470 μm)	424.0 to 491.2
Green (representative, 520 μm)	491.2 to 575.0
Maximum visibility	556
Yellow (representative, 580 μm)	575.0 to 585.0
Orange (representative, 600 μm)	585.0 to 647.0
Red (representative, 650 μm)	647.0 to 700.0
Infrared	>700
Hertzian waves	$>0.22\times10^{6}$

[a]Limit of Sun's ultraviolet at Earth's surface, 292.

Organic materials contain the elements carbon and (usually) hydrogen as a key part of their structures, and they are usually derived from living things. Polymers, natural resins, soils, some foods, and living organisms are organic solids. Liquid lubricants, fuels, chemicals, oils, paints, and some foods are organic liquids. Hydrocarbons and carbon oxides are organic gases.

Inorganic materials are those substances not derived from living things. Solids such as metals, ceramics, composites, glasses, clays, cements, sand, and rock; liquids such as water, acids, bases, and drugs; and gases such as chlorine, argon, and helium are all inorganic.

Wavelengths of various radiations vary from less than 1 nm (high-energy radiation such as gamma rays and x rays) to a few hundred nanometers or more (e.g, infrared), as shown in Table 2.5. In nuclear plants, space systems such as communication satellites, and bridges solid lubricants are exposed to radiation over long times. The resistance of various solid lubricants to extreme temperatures has significantly expedited their development. Various types of solid lubricant perform well against thermal radiation at temperatures in the cryogenic region and up to 1000 °C.

Vacuum ranges involved in industrial vacuum processes vary from low to ultrahigh vacuum (Fig. 2.51). For example, a steel degassing process requires a vacuum range of 10 to 10^3 Pa, and a metal sputtering process requires a vacuum range of 10^{-7} to 10^{-4} Pa. Solid lubricants offer one of the most promising methods of space system lubrication in the vacuum range 10^{-4} to 10^{-9} Pa.

2.4.2 Particulates and Fine Dusts

The environment can be polluted by particulates and fine dusts created by people's activities and by nature [2.43]. In 1974 the U.S. Environmental Protection Agency set a total suspended particulates standard of 75 mg/m^3 as a

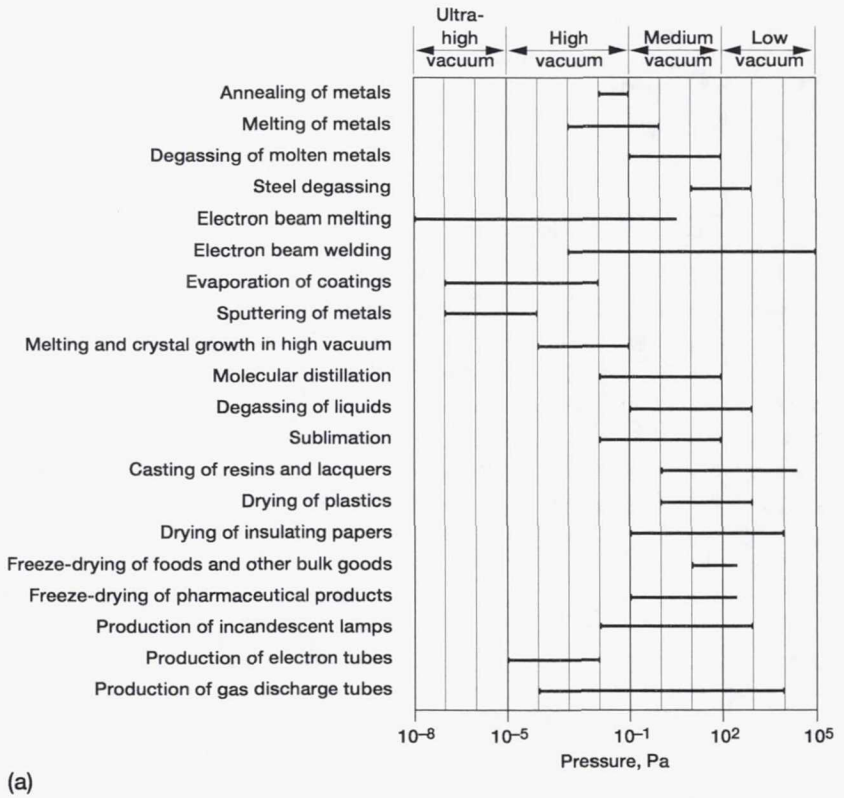

(a)

Figure 2.51.—Fields of application of high vacuum. (a) Industrial applications. (b) Research and development applications.

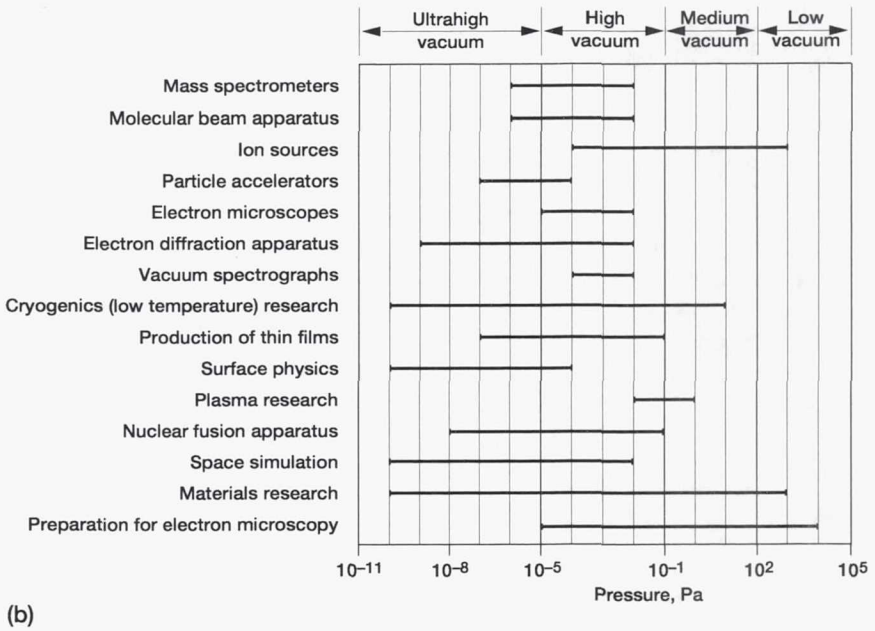

(b)

Figure 2.51.—Concluded. (b) Research and development applications.

primary standard for the protection of public health. A secondary standard of 60 mg/m^3 was established as necessary to protect the public welfare. Actual measurements at background sites have consistently shown counts of about 35 mg/m^3. Measurements at national monitoring sites run close to the tolerance level of 75 mg/m^3. Small particles in polluted air are controlled hardly at all by gravitational forces. Once they enter the atmosphere, their residence time is likely to range from a month to several years. The suspended atmospheric particles are of four general types. The first is the light ions produced in the air by cosmic rays and radioactivity. They consist of small aggregates of molecules having dimensions up to a few molecular diameters. The second important type of particle consists of the so-called Aitken nuclei. These particles range in radius from 2 nm up to 2 mm. They are prevalent near the Earth's surface, particularly near cities. As a rule of thumb one anticipates finding 100 000 of these particles per cubic centimeter in a large city, 10 000/cm^3 in the country, and 1000/cm^3 at sea. The numbers decrease with increasing altitude and only 10% of the surface populations are found at an altitude of 7000 m. The fine-particle pollution of the air is largely composed of these nuclei. The third type of atmospheric particle is the cloud droplet having a radius from 1 to 50 mm. Finally, cloud droplets associate to form raindrops or snowflakes that fall at velocities dependent on their size.

Particles in the environment are involved in virtually all tribological situations that produce contamination, abrasive wear, corrosion, and erosion. They adsorb on surfaces and change surface properties and tribological behavior. Fine particles in the atmosphere may also influence lifetime and reliability in all mechanical systems with moving parts. Despite their importance they have not received the same attention as other areas of tribology.

2.5 Concluding Remarks

As soon as we are confronted with a system where surface properties are involved, we are in trouble. The difficulty with surfaces in most practical situations is that conditions above, at, and below the engineering surface are extremely complex.

The properties of engineering surfaces in tribological applications can be determined by material and surface analytical techniques. Material and surface analyses are evolutionary disciplines. A number of analysis techniques are available for studying tribological surfaces and coatings, including solid-film lubricants, from the atomic and electronic levels to macroscopic, engineering component levels. Such techniques include a variety of physical, chemical, metallurgical, and mechanical characterizations. They can provide information that will allow us to select the materials, lubricants, coatings, environments, and surface treatments best suited for a particular tribological application.

References

2.1 P.F. Kane and G.B. Larrabee, *Characterization of Solid Surfaces*, Plenum Press, New York, 1974.

2.2 F.P. Bowden and D. Tabor, *The Friction and Lubrication of Solids—Part 1*, Clarendon Press, Oxford, UK, 1954.

2.3 F.P. Bowden and D. Tabor, *The Friction and Lubrication of Solids—Part 2*, Clarendon Press, Oxford, UK, 1964.

2.4 *Surface Analysis and Pretreatment of Plastics and Metals* (D.M. Brewis, ed.), Macmillan Publishing Co., New York, 1982.

2.5 D. Briggs and M.P. Seah, *Practical Surface Analysis: By Auger and X-Ray Photo-Electron Spectroscopy*, Vol. 1, John Wiley & Sons, New York,1983.

2.6 D.H. Buckley, *Surface Effects in Adhesion, Friction, Wear, and Lubrication*, Elsevier Scientific Publishing Co., New York, 1981.

2.7 Y.W. Chung and H.S. Cheng, *Advances in Engineering Tribology*, STLE SP–31, Society of Tribologists and Lubrication Engineers, Park Ridge, IL, 1991.

2.8 Y.W. Chung, A.M. Homola, and G.B. Street, *Surface Science Investigations in Tribology: Experimental Approaches*, Developed From the 201st National Meeting of the American Chemical Society Symposium, American Chemical Society, Washington, DC, 1992.

2.9 W.A. Glaeser, *Characterization of Tribological Materials*, Butterworth-Heinemann, Boston, MA, 1993.

2.10 C.R. Brundle, C.A. Evans, Jr., and S. Wilson, Jr., *Encyclopedia of Materials Characterization: Surfaces, Interfaces, Thin Films*, Butterworth-Heinemann, Boston, MA, 1992.

2.11 K. Miyoshi and Y.W. Chung, *Surface Diagnostics in Tribology: Fundamental Principles and Applications*, World Scientific Publishing Co., River Edge, NJ, 1993.

2.12 K.F. Dufrane and W.A. Glaeser, Rolling-contact deformation of MgO single crystals, *Wear 37*: 21–32 (1976).

2.13 R.P. Steijn, On the wear of sapphire, *J. Appl. Phys. 32, 10*: 1951–1958 (1961).

2.14 K. Tanaka, K. Miyoshi, Y. Miyao, and T. Murayama, Friction and deformation of Mn-Zn ferrite single crystals, *Proceedings of the JSLE–ASLE International Lubrication Conference* (T. Sakurai, ed.), Elsevier Scientific Publishing Co., Amsterdam, 1976.

2.15 K. Miyoshi and D.H. Buckley, Friction, deformation, and fracture of single-crystal silicon carbide, *ASLE Trans. 22*: 79–90 (1979).

2.16 H. Ishigaki, K. Miyoshi, and D.H. Buckley, Influence of corrosive solutions on microhardness and chemistry of magnesium oxide {001} surface, NASA TP–2040 (1982).

2.17 K. Miyoshi, D.H. Buckley, G.W.P. Rengstorff, and H. Ishigaki, Surface effects of corrosive media on hardness, friction, and wear of materials, *Ind. Eng. Chem. Prod. Res. Dev. 24, 3*: 425–431 (1985).

2.18 S. Hattori, K. Miyoshi, D.H. Buckley, and T. Okada, Plastic deformation of a magnesium oxide {001} surface produced by cavitation, *Lubric. Eng. 44,1*: 53–58 (1988).

2.19 J. Narayan, The characterization of the damage introduced during micro-erosion of MgO single crystals, *Wear 25*: 99–109 (1973).

2.20 J. Narayan, Physical properties of a ⟨100⟩ dislocation in magnesium oxide, *J. Appl. Phys. 57, 8*: 2703–2716 (1985).

2.21 P.T.B. Shaffer, Effect of crystal orientation on hardness of silicon carbide, *J. Am. Ceram. Soc. 47, 9*: 466 (1964).

2.22 O.O. Adewoye, G.R. Sawyer, J.W. Edington, and T.F. Page, Structural studies of surface deformation in MgO, SiC, and Si_3N_4, Annual Technical Report AD–A008993, Cambridge University Press, Cambridge, England, 1974.

2.23 A.G. Guy, Deformation of materials, *Introduction to Materials Science*, McGraw-Hill, New York, 1972, pp. 399–451.

2.24 R.M. Brick, A.W. Pense, and R.B. Gordon, Strengthening mechanisms; deformation hardening and annealing, *Structure and Properties of Engineering Materials*, McGraw-Hill, New York, 1977, pp. 69–92.

2.25 S. Amelinckx, G. Strumane, and W.W. Webb, Dislocations in silicon carbide, *J. Appl. Phys. 31, 8*: 1359–1370 (1960).

2.26 C.A. Brookes, J.B. O'Neill, and B.A.W. Redfern, Anisotropy in the hardness of single crystals, *Proc. R. Soc. London, A 322*: 73–88 (1971).

2.27 F.W. Daniels and C.G. Dunn, The effect of orientation on Knoop hardness of single crystals of zinc and silicon ferrite, *Trans. Am. Soc. Met. 41*: 419–442 (1949).

2.28 D.N. French and D.A. Thomas, Hardness anisotropy and slip in WC crystals, *Trans. Metall. Soc. AIME 233*: 950–952 (May 1965).

2.29 D.H. Buckley and K. Miyoshi, Friction and wear of ceramics,*Wear 100*: 333–353 (1984).

2.30 J.B.P. Williamson, The shape of surfaces, *CRC Handbook of Lubrication* (E.R. Booser, ed.), CRC Press Inc., Boca Raton, FL, Vol. II, 1984, pp. 3–16.

2.31 Y.W. Chung, Characterization of topography of engineering surfaces, *Surface Diagnostics in Tribology: Fundamental Principles and Applications* (K. Miyoshi and Y.W. Chung, eds.), World Scientific Publishing, River Edge, NJ, 1993, pp. 33–46.

2.32 R.S. Howland, J. Okagaki, and L. Mitobe, How To Buy a Scanning Probe Microscope, Park Scientific Instruments, 1993.

2.33 T. Tsukizoe, *Precision Metrology*, Yokkendo Publishing, Tokyo, Japan, 1970, pp. 180–199.

2.34 T. Hisakado, On the mechanism of contact between solid surfaces, *Bull. JSME 12, 54*: 1519–1527, 1528–1536 (1969).

2.35 T. Tsukizoe, T. Hisakado, and K. Miyoshi, Effects of surface roughness on shrinkage fits, *Bull. JSME 17, 105*: 359–366 (1974).

2.36 Y. Kumada, K. Hashizume, and Y. Kimura, Performance of plain bearings with circumferential microgrooves, *Tribol. Trans 39*: 81–86 (1996).

2.37 D.H. Buckley and K. Miyoshi, Tribological properties of structural ceramics, *Structural Ceramics* (J.B. Wachtman, Jr., ed.), Academic Press, Boston, MA, 1989, pp. 203–365.

2.38 P.G. Lurie and J.M. Wilson, The diamond surface, *Surf. Sci. 65*: 476–498, North-Holland Publishing Co. (1976).

2.39 S. Evans, R.G. Pritchard, and J.M. Thomas, Escape depths of x-ray (Mg K_{α})-induced photoelectrons and relative photoionization cross sections for the 3p subshell of the elements of the first long period, *J. Phys. C. 10, 13*: 2483–2498 (July 1977).

2.40 P. Cadman, S. Evans, J.D. Scott, and J.M. Thomas, Determination of relative electron inelastic mean free paths (escape depths) and photoionization cross sections by x-ray photoelectron spectroscopy, *J. Chem. Soc., Faraday Trans. II 71, 10*:1777–1784 (1975).

2.41 J.T. Norton and G.T. Cameron, Sr., eds., Electron optical and x-ray instrumentation for research, product assurance and quality control, Amray Technical Bulletins, Vol. 2, No. 1, Amray, Inc., Bedford, MA, Jan. 1986.

2.42 K.G. Budinski, *Engineering Materials Properties and Selection*, Prentice Hall, Englewood Cliffs, NJ, 1992.

2.43 M. Sittig, *Particulates and Fine Dust Removal Processes and Equipment*, Noyes Data Corp., Park Ridge, NJ, 1977.

2.44 H. Hantsche, Comparison of basic principles of the surface-specific analytical methods AES/SAM, ESCA(XP), SIMS and ISS with x-ray microanalysis, *Scanning 11, 6*: 257–280, FACM, Inc., Mahwah, NJ (1989).

REPORT DOCUMENTATION PAGE

Form Approved
OMB No. 0704-0188

Public reporting burden for this collection of information is estimated to average 1 hour per response, including the time for reviewing instructions, searching existing data sources, gathering and maintaining the data needed, and completing and reviewing the collection of information. Send comments regarding this burden estimate or any other aspect of this collection of information, including suggestions for reducing this burden, to Washington Headquarters Services, Directorate for Information Operations and Reports, 1215 Jefferson Davis Highway, Suite 1204, Arlington, VA 22202-4302, and to the Office of Management and Budget, Paperwork Reduction Project (0704-0188), Washington, DC 20503.

1. AGENCY USE ONLY (*Leave blank*)	2. REPORT DATE	3. REPORT TYPE AND DATES COVERED
	July 1998	Technical Memorandum

4. TITLE AND SUBTITLE

Solid Lubrication Fundamentals and Applications
Characterization of Solid Surfaces

5. FUNDING NUMBERS

WU–505–63–5A

6. AUTHOR(S)

Kazuhisa Miyoshi

7. PERFORMING ORGANIZATION NAME(S) AND ADDRESS(ES)

National Aeronautics and Space Administration
Lewis Research Center
Cleveland, Ohio 44135–3191

8. PERFORMING ORGANIZATION REPORT NUMBER

E–9863–2

9. SPONSORING/MONITORING AGENCY NAME(S) AND ADDRESS(ES)

National Aeronautics and Space Administration
Washington, DC 20546–0001

10. SPONSORING/MONITORING AGENCY REPORT NUMBER

NASA TM—1998-107249
CH2

11. SUPPLEMENTARY NOTES

Responsible person, Kazuhisa Miyoshi, organization code 5140, (216) 433–6078.

12a. DISTRIBUTION/AVAILABILITY STATEMENT

Unclassified - Unlimited
Subject Category: 27 Distribution: Nonstandard

This publication is available from the NASA Center for AeroSpace Information, (301) 621–0390.

12b. DISTRIBUTION CODE

13. ABSTRACT ***(Maximum 200 words)***

This chapter describes powerful analytical techniques capable of sampling tribological surfaces and solid-film lubricants. Some of these techniques may also be used to determine the locus of failure in a bonded structure or coated substrate; such information is important when seeking improved adhesion between a solid-film lubricant and a substrate and when seeking improved performance and long life expectancy of solid lubricants. Many examples are given here and throughout the book on the nature and character of solid surfaces and their significance in lubrication, friction, and wear. The analytical techniques used include the late spectroscopic methods.

14. SUBJECT TERMS

Solid lubrication; Coatings; Tribology fundamentals; Applications

15. NUMBER OF PAGES

84

16. PRICE CODE

A05

17. SECURITY CLASSIFICATION OF REPORT	18. SECURITY CLASSIFICATION OF THIS PAGE	19. SECURITY CLASSIFICATION OF ABSTRACT	20. LIMITATION OF ABSTRACT
Unclassified	Unclassified	Unclassified	